CENTRO DE INVESTIGACIONES
EN OPTICA, A.C.

“IMPLEMENTATION OF A PHOTON PAIRS SPECTRAL CHARACTERIZATION SYSTEM”

Tesis que para obtener el grado de Maestro en Ciencias (Óptica)

Presenta: Oscar Alejandro Ramírez Espinosa

Director de Tesis: Dr. Roberto Ramírez Alarcón

León · Guanajuato · México
Noviembre de 2023

Acknowledgment

This work would not have been possible without the knowledge and patience of Dr. Roberto Ramírez Alarcón, for which I am extremely grateful. I'd also like to extend my thanks to my colleague, Juan Samuel S. Durán Gómez, for generously sharing his expertise in experimental techniques. I thank CONACYT for the financial support that was provided to me to carry out this work.

Also want to thank my mother Marta Catalina Ramírez Espinosa, for believe, support and love towards me. Even with ups and downs you have always supported me, thanks. To all my friends, to be my support when I was in the lowest, for bring joy all the time we spend together. Io thanks to see the best of me even when I can't, to inspire me.

Contents

1 Introduction **1**

2 Theoretical fundamentals **4**
2.1 Optical Fiber 4
2.2 Non-linear processes 7
2.3 Four-Wave Mixing 8
2.4 Cross-Polarized 10
2.5 Counter-Propagation 14

3 Simulation **18**
3.1 Propagation constant 18
3.2 Cross-Polarized 19
3.3 Counter-propagation 23

4 Experimental development **25**
4.1 Fiber emission 25
4.2 Spectral Characterization 33
4.3 ICCD measurement 36

5 Discussion and conclusions **38**

Abstract

In this study, a comprehensive setup for the spectral characterization of photon pairs is presented, enabling the determination of the degree of correlation between them, with the purpose of studying the correlation between the frequencies of photon pairs generated by non-linear processes. The characterization system used consist of two Avalanche Photodiodes (APD), that count the number of photons that arrive, a IDQ800 that register the number of photons pairs that arrive in a window of time, and two monochromators that help to select the spectral components that arrive to the APDs. The intention of building the spectral characterization system is to measure the intriguing process of Counter-Propagation Four-Wave Mixing, where the theory gives a configuration in which the factorability of the state is always satisfied, and the phase-matching condition is consistently satisfied, due to technical problems this process could not be measured. The system was also calibrated with the Spontaneous Four-Wave Mixing Cross-Polarized case in a birefringence fiber model (HB800G). For this case, measurements of the spectral correlations were performed, which show a high correlation between the photon pair. Simulations of both cases of SFWM were made, in order to compare with the experimental measurements. For the Counter-Polarized process, the simulations have an excellent agreement with the experimental results and there is no factorizable state. However, for the Counter-Propagation one, there is a factorizable state.

Chapter 1

Introduction

The field of quantum photonics has witnessed significant advancement in recent years, leading to the integration of quantum technologies in various applications worldwide. Notable examples of these applications include quantum computing [1, 2], quantum encryption [3], and quantum teleportation [4]. The ongoing development in quantum photonics [5–7] have been instrumental in driving the second quantum revolution, with resources such as entanglement and non-locality .

The area of interest for this work is photonics, with a specific focus on the photons generated by nonlinear processes. Nonlinear optical phenomena were first observed approximately four years after the invention of the laser [8]. These processes typically require optical fields with high-energy density to stimulate the generation of new photons. The first reported nonlinear process was Second Harmonic Generation (SHG), where two photons with frequency ω are absorbed, resulting in the generation of a photon with frequency 2ω [9]. Other processes of high relevance include Spontaneous Parametric Down Conversion (SPDC) [10, 11], Spontaneous Four Wave Mixing (SFWM) [12], and Two-Photon Absorption (TPA) [13]. In these processes, the generated photons have correlations. These correlations can include various degrees of freedom, such as propagation modes [14], orbital angular momentum (OAM) [15], or frequency [16]. In this work the focus will be the spectral correlation, meaning the correlations on frequency.

These non-lineal processes can be conducted in various media, including crystals, optical fibers, and waveguides, among others. They often exhibit spectral correlations due to the inherent nature of generation from the same physical process. This spectral correlation can be tailored or modified based on the specific conditions and properties of the medium used. A prime example of such a medium is Photonic Crystal Fiber (PCF) [17], which contains an array of micro-structured holes that can significantly alter the propagation and dispersion properties of light. This capability allows for the customization of photons generated by processes like Spontaneous Four Wave Mixing (SFWM), enabling the production of either factorizable states or highly correlated states as required for specific quantum applications [18].

In integrated photonics [19], the commonly used non-linear process for generating photon pairs is SFWM, which is a third-order process where two pump photons are annihilated in order to generate a pair of photons known as signal and idler. While

other non-linear processes like Spontaneous Parametric Down Conversion (SPDC) also generate photon pairs, they are typically produced in crystals and may incur in coupling losses when connected to integrated systems. SFWM can be generated inside an optical fiber or a waveguide and can be tailored by modifying the fiber structure [17, 20] or by adjusting the pump characteristics [21]. Some of the most intriguing properties of SFWM in fibers are its quadratic photon pairs flux dependence with the pump power [22]. Depending on the fiber length, it is possible to achieve a large interaction length, enhancing photon pairs production flux. Additionally, SFWM exhibits an effective non-linearity that can be scaled down by reducing the transverse mode area [19].

The particular case of co-polarized Counter-Propagation Spontaneous Four-Wave Mixing (CP-SFWM) presents an intriguing scenario where any single-mode fiber can be employed to produce photon pairs characterized by factorable states. In this case of SFWM the factorability of the state is consistently maintained, and the phase-matching condition is always met, as long as all the waves involved are within the same dispersion regimen. For CP-SFWM, the optical fiber is pumped from both ends, resulting in generated photons that share the same wavelengths as the pumps but which propagates in opposite directions [23].

Nevertheless, as far as we know, experimental implementation of CP-SFWM process in an optical fiber has not been reported, since the original scheme considered laser pumps and produced photons wavelengths in the Si detection range, making extremely hard to discriminate the photon's signal in the detection system from the noise produced by residual pumps, even when extremely efficient spectral filters are employed. A viable scenario which could allow for the demonstration of such an interesting scheme is the production of one photon in the Si detection and the other in the InGaAs detection range. Since current available detectors based in Si are insensible to radiation in the spectral range of detection of an InGaAs detector, and viceversa, the residual noise produced by the pumps can be effectively discriminated by the use of efficient spectral filters aid by the insensibility of the detectors.

A particularly interesting feature of CP-SFWM is when one of the pumps is pulsed while the other is a continuous-wave (CW). In this configuration, the photon generated with the wavelength of the CW pump exhibits a narrow spectral width which narrows as the fiber's interaction lenght increases. This feature is of special interest for the interaction with atomic transitions in applications for quantum memories [24, 25], simplifying greatly the photon pairs source design which typically require the implementation of SFMW sources in elaborated integrated or bulk resonator configurations. Specifically, within our research group, the creation of a quantum memory integrated full on fiber is in mind, for this a transition of interest is around 1532 nm to interact with the $^4I_{15/2} \rightarrow^4 I_{13/2}$ transition of erbium doped fiber. Then, in this work we extended the reported model of CP-SFWM, considering a pulsed pump in the 800 nm range and a CW pump around 1532 nm, in order to produce one photon to match the wavelength and the spectral bandwidth of Erbium ions in a quantum memory application [25].

In order to experimentally demonstrate the elusive process of CP-SFWM, we need to build and characterize an optimized SFWM detection system, which allows for the

efficient detection and spectral characterizarion of the produced photons, including the hard to achieve measurement of the Joint Spectral Intensity (JSI) function which, as will be explained in the sections ahead, essentially defines all the properties of the photon pair's quantum state. Then, as the experimental section of this thesis we present the design and implementation of a SFWM measurement system.

To validate the system's functionality, we implemented a well-understood SFMW scheme, which is the co-propagating Cross-Polarized Spontaneous Four-Wave Mixing (XP-SFMW) configuration. The advantage of this case lies in its simplicity to mitigate noise in measurements due to the orthogonal polarization of the pumps compared to the generated photon pairs. Additionally, since this process has been previously studied, it facilitates a comparison of the obtained results with those presented in existing literature [26, 27].

The characterization system functions by detecting each photon using Avalanche Photodiodes (APDs) and counting the time coincidence between them with an IDQ800. This coincidence arises because photons generated by SFWM travel the same distance and arrive at approximately the same time, indicating the generation of a photon pair. Utilizing two monochromators, a spectral component is selected on each side to check if, at certain wavelengths, there is the generation of photon pairs. This allows the recreation of the correlation between the two photons. The objective is to understand the properties of the quantum states generated. Understanding the correlation between the two photons is crucial in various applications, such as spectroscopy [18], where factorizable states are required. This enables the use of both photons to interact with the material being analyzed without the limitations imposed by high correlations between them.

In the following sections, we will delve into the theory of Spontaneous Four Wave Mixing in optical fibers for the cases of Counter-Propagated co-polarized and co-propagating Cross-Polarized. This theoretical foundation serves as a crucial backdrop for understanding the subsequent simulations. Moving forward, it will unveil the extensive experimental work carried out. This includes the meticulous measurements of spectral and coincidence counts, essential for extracting the correlation structure of photon pairs generated within a HB800G bow-tie fiber. Additionally, it will be exploring the assembly of the characterization system and some alternative methods to realize the measurement of the Joint Spectral Intensity.

The culmination of this work will involve a thorough comparison of theoretical results with experimental measurements. We will also engage in a brief but insightful discussion of the system, future research possibilities, and potential avenues for system improvement.

Chapter 2

Theoretical fundamentals

This chapter introduces the theory of Spontaneous Four Wave Mixing (SFWM) in optical fiber, with a focus on two specific cases: Cross-Polarized and Counter-Propagated. The discussion begins with the propagation of light inside an optical fiber, followed by an exploration of non-linear optics and the phenomenon of Four Wave Mixing. The chapter then delves into the quantum analysis of the Cross-Polarized and Counter-Propagated cases, aiming to derive the Joint Spectral Intensity, a quantum parameter that brings information of the correlation between the frequencies of the photons generated.

2.1 Optical Fiber

To understand the non-linear process of SFWM it is necessary to understand the propagation of light in the medium. This section focuses on conducting a mathematical analysis of the electromagnetic fields inside an optical fiber.

An optical fiber is essentially a cylindrical structure composed of glass, typically Fused Silica. It comprises an inner region known as the core, which is encircled by an outer region referred to as the cladding [28]. The specific type of fiber under analysis here is a step index fiber, and its structure can be observed in Figure 2.1. There are other types of optic fibers designed for different applications [29].

Maxwell's equations in media without sources are the starting point in the analysis of the propagation properties of the light inside the optic fiber:

$$\begin{aligned} \vec{\nabla} \times \vec{E}(\vec{r},t) &= -\frac{\partial \vec{B}(\vec{r},t)}{\partial t}, \\ \vec{\nabla} \times \vec{H}(\vec{r},t) &= \frac{\partial \vec{D}(\vec{r},t)}{\partial t}, \\ \vec{\nabla} \cdot \vec{H}(\vec{r},t) &= 0, \\ \vec{\nabla} \cdot \vec{D}(\vec{r},t) &= 0, \end{aligned} \tag{2.1}$$

where $\vec{E}$ is the electric field, $\vec{H}$ is the magnetic field, $\vec{D} = \epsilon_0 \vec{E} + \vec{P} = \epsilon \vec{E}$ is the electric displacement, $\vec{B} = \mu_0 \vec{H} + \vec{M}$ is the magnetic flux density, where for non magnetic

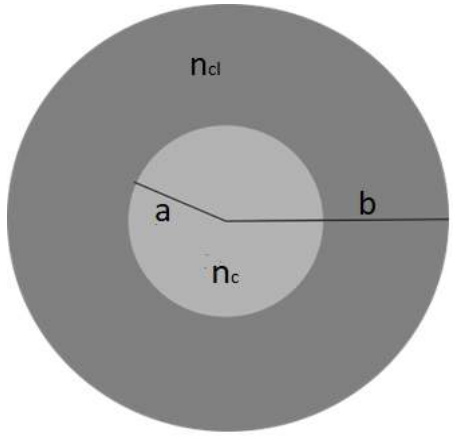

Figure 2.1: Structure of a Step Index Fiber.Where a is the core radius, b is the cladding radius, n_c is the refractive index of the core and n_{cl} is the refractive index of the cladding.

mediums the magnetism is $\vec{M} = 0$. Applying the curl operator to the first equation yields:

$$\vec{\nabla} \times \vec{\nabla} \times \vec{E}(\vec{r}, t) = -\vec{\nabla} \times \frac{\partial \vec{B}(\vec{r}, t)}{\partial t}.$$

This equation can be rearrange as follows:

$$\vec{\nabla}(\vec{\nabla} \cdot \vec{E}) - \vec{\nabla}^2 \vec{E} = -\mu_0 \frac{\partial}{\partial t}(\vec{\nabla} \times \vec{H}),$$

next by using that $\vec{\nabla} \cdot \vec{E} = 0$ y $\vec{\nabla} \times \vec{H} = \frac{\partial \epsilon \vec{E}}{\partial t}$ one obtains:

$$\vec{\nabla}^2 \vec{E}(\vec{r}, t) = \mu_0 \epsilon \frac{\partial^2 \vec{E}(\vec{r}, t)}{\partial t^2}. \tag{2.2}$$

This wave differential equation can be rewritten in the frequency domain to simplify the analysis

$$\vec{\nabla}^2 \tilde{E}(\vec{r}, \omega) = \mu_0 \epsilon \omega^2 \tilde{E}(\vec{r}, \omega), \tag{2.3}$$

with

$$\vec{E}(\vec{r}, \omega) = \frac{1}{2\pi} \int_{-\infty}^{\infty} \tilde{E}(\vec{r}, t) e^{-i\omega t} dt.$$

Due to geometrical structure of the waveguide, cylindrical coordinates are utilized. By expanding the Laplacian operator in those coordinates, Eq. 2.3 can be expressed as:

$$\frac{\partial^2 \tilde{E}(\vec{r}, \omega)}{\partial r^2} + \frac{1}{r} \frac{\partial \tilde{E}(\vec{r}, \omega)}{\partial r} + \frac{1}{r^2} \frac{\partial^2 \tilde{E}(\vec{r}, \omega)}{\partial \phi^2} + \frac{\partial^2 \tilde{E}(\vec{r}, \omega)}{\partial z^2} + n^2 k_0^2 \tilde{E}(\vec{r}, \omega) = 0, \tag{2.4}$$

where $n^2 k_0^2 = \omega^2 / v^2$. Similarly, for magnetic field one gets the following equation:

$$\frac{\partial^2 \tilde{H}(\vec{r}, \omega)}{\partial r^2} + \frac{1}{r} \frac{\partial \tilde{H}(\vec{r}, \omega)}{\partial r} + \frac{1}{r^2} \frac{\partial^2 \tilde{H}(\vec{r}, \omega)}{\partial \phi^2} + \frac{\partial^2 \tilde{H}(\vec{r}, \omega)}{\partial z^2} + n^2 k_0^2 \tilde{H}(\vec{r}, \omega) = 0\cdot \tag{2.5}$$

The two vectorial differential equations 2.4 and 2.5 have six components, three of electric field and the other three in the magnetic field. However, the fields are subject to

Maxwell's equations, which restrict the system to only two degrees of freedom. To solve for the fields, a separable solution is proposed for the components in the propagation direction z:

$$\tilde{E}_z(r,\phi,z,\omega) = W(\omega)R(r)e^{i(m\phi+\psi)}e^{i\beta z}, \tag{2.6}$$

where β is the propagation constant, m is a integer, and ψ is a functional form because of the cylindrical symmetry. By using the electric field with this form in Eq. 2.4 gives:

$$\frac{d^2R(r)}{dr^2} + \frac{1}{r}\frac{dR(r)}{dr} + \left(n^2k_0^2 - \beta^2 - \frac{m^2}{r^2}\right)R(r) = 0\cdot \tag{2.7}$$

The differential equation derived for the electric field has the same structure as the Bessel differential equation, indicating that the solutions are Bessel functions. Specifically, in the core of the waveguide, Bessel functions of the first kind J_m are used, while in the cladding, modified Bessel functions of the second kind K_m are used. Consequently, the electric and magnetic fields can be expressed as follows:

$$\begin{aligned}
\tilde{E}_z &= \begin{cases} C_1W(\omega)J_m(pr)e^{i(m\phi+\psi)}e^{i\beta z}\ , & r<a \\ C_2W(\omega)K_m(qr)e^{i(m\phi+\psi)}e^{i\beta z}\ , & r>a \end{cases} \\
\tilde{H}_z &= \begin{cases} C_3W_h(\omega)J_m(pr)e^{i(m\phi+\psi)}e^{i\beta z}\ , & r<a \\ C_4W_h(\omega)K_m(qr)e^{i(m\phi+\psi)}e^{i\beta z}\ , & r>a \end{cases}
\end{aligned} \tag{2.8}$$

where $p = \sqrt{n_c^2k_0^2 - \beta^2}$ y $q = \sqrt{\beta^2 - n_{cl}^2k_0^2}$. By substituting the z component into Eqs. 2.1, we obtain the radial and angular components in the following forms:

$$\begin{aligned}
\tilde{E}_r &= \begin{cases} -\frac{iW(\omega)}{p^2}\left[C_1\beta pJ_m'(pr) + C_3\omega\mu_0\frac{m}{r}J_m(pr)\right]cos(m\theta+\psi)\ , & r<a \\ \frac{iW(\omega)}{q^2}\left[C_1\beta qK_m'(qr) + C_3\omega\mu_0\frac{m}{r}K_m(qr)\right]\frac{J_m(u)}{K_m(w)}cos(m\theta+\psi)\ , & r>a \end{cases} \\
\tilde{E}_\theta &= \begin{cases} -\frac{iW(\omega)}{p^2}\left[-C_1\beta\frac{m}{r}J_m(pr) - C_3\omega\mu_0pJ_m'(pr)\right]\sin(m\theta+\psi) & r<a \\ \frac{iW(\omega)}{q^2}\left[-C_1\beta\frac{m}{r}K_m(qr) - C_3\omega\mu_0K_m'(qr)\right]\frac{J_m(u)}{K_m(w)}\sin(m\theta+\psi)\ , & r>a \end{cases}
\end{aligned} \tag{2.9}$$

$$\begin{aligned}
\tilde{H}_r &= \begin{cases} -\frac{iW(\omega)}{p^2}\left[C_1\omega\epsilon_0n_c^2\frac{m}{a}J_m(pr) + C_3\beta pJ_m'(pr)\right]\sin(m\theta+\psi)\ , & r<a \\ \frac{iW(\omega)}{q^2}\left[C_1\omega\epsilon_0n_{cl}^2\frac{m}{r}K_m(qr) + C_3\beta qK_m'(qr)\right]\frac{J_m(u)}{K_m(w)}\sin(m\theta+\phi)\ , & r>a \end{cases} \\
\tilde{H}_\theta &= \begin{cases} -\frac{iW(\omega)}{p^2}\left[C_1\omega\epsilon_0n_c^2pJ_m'(pr) + C_3\beta\frac{m}{r}J_m(pr)\right]\cos(m\theta+\psi)\ , & r<a \\ \frac{iW(\omega)}{q}\left[C_1\omega\epsilon_0n_{cl}^2qK_m'(qr) + C_3\beta\frac{m}{r}K_m(qr)\right]\frac{J_m(u)}{K_m(qr)}\cos(m\theta+\psi)\ , & r<a \end{cases}
\end{aligned} \tag{2.10}$$

Taking into consideration the boundary conditions for the angular coordinates of the two fields at $r = a$, two equalities are obtain:

$$C_1\beta\left[\frac{1}{u^2} + \frac{1}{w^2}\right] = -C_3\mu\left[\frac{J_m'(U)}{uJ_m(U)} + \frac{K_m'(W)}{wK_m(W)}\right],$$

$$-C_1w\epsilon_0\left[n_c^2\frac{J_m'(U)}{uJ_m(U)} + n_{cl}^2\frac{K_m'(W)}{wJ_m(W)}\right] = C_3\beta m\left(\frac{1}{u^2} + \frac{1}{w^2}\right).$$

Where $U = pr$, $W = wr$. On performing the product of those two equations

$$\left[\frac{J_m'(U)}{uJ_m(U)} + \frac{K_m'(U)}{uK_m(W)}\right]\left[n_c^2l\frac{J_m'(U)}{uJ_m(U)} + n_c\frac{K_m'(W)}{wK_m(W)}\right] = m^2\left(\frac{n_c^2}{u^2} + \frac{n_{cl}^2}{w^2}\right).$$

By rearranging the equation given in [30], is obtain:

$$\left[\frac{J'_m(U)}{UJ_m(U)} + \frac{K'_m(W)}{WK_m(W)}\right]\left[\frac{J'_m(U)}{UJ_m(U)} + \frac{n_c^2}{n_{cl}^2}\frac{K'_m(W)}{WK_m(W)}\right] = \left(\frac{m\beta}{n_c k_0}\right)^2\left(\frac{V}{UW}\right)^4, \quad (2.11)$$

where $V = \sqrt{p^2 + q^2}$. The parameter V, also known as normalized frequency, indicates the number of modes that can propagate in the fiber [30]. This equation is known as the characteristic equation of the optical fiber, and when solved, it gives the propagation constant β of the fiber.

2.2 Non-linear processes

Non-linear optical phenomenon refers to the effects that occur when light interacts with a material, and the response of the material is not proportional to the intensity of the light [31]. This interaction occurs because the atomic elements of the material are excited by the photons that impinge upon them, leading to a change in the material's properties.

Non-linear effects in optics are commonly expressed in terms of polarization. In linear circumstances, polarization is directly proportional to the electric field, and the proportion constants are the electric susceptibility of the medium $\chi^{(1)}$ and the electric permeability in a vacuum ϵ_0. However, in non-linear optics, this linear relationship is just the first term of a potential series. Each element of this series is the polarization of a different order, and it represents a higher order response of the material to the incident light. This is express as [31]:

$$\begin{aligned} \vec{P}(t) = \epsilon_0(\chi^{(1)} \cdot \vec{E}(t) + \chi^{(2)} : \vec{E}(t)\vec{E}(t) + \chi^{(3)} \vdots \vec{E}(t)\vec{E}(t)\vec{E}(t) + \cdots), \\ \vec{P}(t) = \vec{P}^{(1)}(t) + \vec{P}^{(2)}(t) + \vec{P}^{(3)}(t) + \cdots, \end{aligned} \quad (2.12)$$

In isotropic media, such as the fused silica used in this study, the second-order susceptibility can typically be neglected in comparison to third-order processes [22]. In most cases, the energy density of the incident light is not sufficient to induce higher-order processes, and therefore, only third-order processes need to be considered. As a result, the polarization can be expressed as:

$$\vec{P}(t) = \vec{P}^{(1)} + \vec{P}^{(3)} = \vec{P}_L + \vec{P}_{NL}. \quad (2.13)$$

To analyze third-order non-linear phenomena, let us start by writing the electric field and polarization as:

$$\vec{E} = \frac{1}{2}\hat{x}\sum_{j=1}^{4} E_j e^{i(\beta_j z - \omega_j t)} + c.c. \quad (2.14)$$

$$\vec{P}_{NL} = \frac{1}{2}\hat{x}\sum_{j=1}^{4} P_j e^{i(\beta_j z - \omega_j t)} + c.c. \quad (2.15)$$

The terms P_j consist of a great amount of terms due to the product of three electrical fields as is imply in Eq. 2.12, giving terms as:

$$
\begin{aligned}
P_4 = \frac{3\epsilon_0}{4}\chi^{(3)}_{xxxx}[|E_4|^2E_4 + 2(|E_1|^2 + |E_2|^2 + |E_3|^2 + |E_3|^2)E_4 \\
+2E_1E_2E_3e^{i[(\beta_1+\beta_2+\beta_3-\beta_4)z-(\omega_1+\omega_2+\omega_3-\omega_4)t]} \\
+2E_1E_2E_3^*e^{i[(\beta_1+\beta_2-\beta_3-\beta_4)z-(\omega_1+\omega_2-\omega_3-\omega_4)t]}] + \cdots,
\end{aligned}
\tag{2.16}
$$

Each term in the polarization expansion represents a different kind of process. For example, the first term represents Self-Phase Modulation, while the second term represents Cross-Self Modulation, which are interactions between a field with itself or with other fields [32]. The remaining terms represent different kinds of FWM, and the efficiency of these processes depends on the phase relation between the fields. In all these processes, energy conservation must be satisfied, leaving the phase term with the propagation constant. This is denote as phase-matching, and only the processes with a phase-matching close to zero are typically observed, while the rest are inefficient and disregarded [31].

2.3 Four-Wave Mixing

As mention earlier, Four Wave Mixing is a third-order process in which four waves interact [22, 32]. The particular case of interest is when two waves are absorbed, and two different waves are created. The analysis begins by using Maxwell's equations, taking into consideration the non-linear polarization P_{NL}.

$$
\nabla^2\vec{E} - \frac{n^2}{c^2}\frac{\partial^2\vec{E}}{\partial t^2} = \mu_0\frac{\partial^2 P_{NL}}{\partial t^2}. \tag{2.17}
$$

Next, the fields are rewritten by using the expressions given in Eq. 2.14 and 2.15 to express them in terms of the electric field. A separable solution is used in the form of $E_j = F_j(x,y)A_j(z)$. Working out the wave equation leads to a set of four coupled equations, which can be integrated over the spatial mode profiles to obtain:

$$
\begin{aligned}
\frac{dA_1}{dz} &= \frac{in_2\omega_1}{c}\left[\left(f_{11}|A_1|^2 + 2\sum_{k\neq 1} f_{1k}|A_k|^2\right)A_1 + 2f_{1234}A_2^*A_3A_4e^{i\Delta kz}\right], \\
\frac{dA_2}{dz} &= \frac{in_2\omega_2}{c}\left[\left(f_{22}|A_2|^2 + 2\sum_{k\neq 2} f_{2k}|A_k|^2\right)A_2 + 2f_{2134}A_1^*A_3A_4e^{i\Delta kz}\right], \\
\frac{dA_3}{dz} &= \frac{in_2\omega_3}{c}\left[\left(f_{33}|A_3|^2 + 2\sum_{k\neq 3} f_{3k}|A_k|^2\right)A_3 + 2f_{3412}A_1A_2A_4^*e^{-i\Delta kz}\right], \\
\frac{dA_4}{dz} &= \frac{in_2\omega_4}{c}\left[\left(f_{44}|A_4|^2 + 2\sum_{k\neq 4} f_{4k}|A_k|^2\right)A_4 + 2f_{4312}A_1A_2A_3^*e^{-i\Delta kz}\right],
\end{aligned}
\tag{2.18}
$$

where $\Delta k = \beta_1 + \beta_2 - \beta_3 - \beta_4$ is the wave-vector mismatch,

$$
f_{jk} = \frac{\iint_{-\infty}^{\infty}|F_j(x,y)|^2|F_k(x,y)|^2dxdy}{(\iint_{-\infty}^{\infty}|F_j(x,y)|^2dxdy)(\iint_{-\infty}^{\infty}|F_k(x,y)|^2dxdy)},
$$

and

$$f_{ijkl} = \frac{\iint_{-\infty}^{\infty} |F_i(x,y)|^2 |F_j(x,y)|^2 |F_k(x,y)|^2 |F_l(x,y)|^2 dxdy}{(\iint_{-\infty}^{\infty} |F_i)|^2 dxdy)(\iint_{-\infty}^{\infty} |F_j|^2 dxdy)(\iint_{-\infty}^{\infty} |F_k|^2 dxdy)(\iint_{-\infty}^{\infty} |F_l k|^2 dxdy)},$$

in Eq. 2.18, the terms that are considered are only the ones that are nearly phase-matched, and the dependence of $\chi^{(3)}$ on the frequency is neglected. The parameter n_2 represents the nonlinear coefficient [33].

To simplify the analysis, it is assumed that the pump waves are much more intense than the other waves and that the overlap integrals are nearly the same, i.e.,

$$f_{ijkl} \approx f_{ij} \approx 1/A_{eff},$$

with this assumption, it is possible to obtain the solution for A_1 and A_2:

$$\begin{aligned} A_1(z) &= A_1(0)e^{i\gamma(P_1+2P_2)z}, \\ A_2(z) &= A_2(0)e^{i\gamma(P_2+2P_1)z}, \end{aligned} \tag{2.19}$$

where $\gamma_j = n_2\omega_j/(cA_{eff}) \approx \gamma$ is the non-linear parameter, $P_j = |A_j(0)|^2$ are the incident pumps power at z=0. It is clear that the solution of the incident fields is not dependent of the created fields, as expected. Substituting these solutions in the other coupled equations, one obtains:

$$\begin{aligned} \frac{dA_3}{dz} &= 2i\gamma[(P_1+P_2)A_3 + A_1(0)A_2(0)e^{-i[\Delta k - 3\gamma(P_1+P_2)]z}A_4^*], \\ \frac{dA_4^*}{dz} &= -2i\gamma[(P_1+P_2)A_4^* + A_1^*(0)A_2^*(0)e^{i[\Delta k - 3\gamma(P_1+P_2)]}A_3]. \end{aligned} \tag{2.20}$$

To solve those equations, the following solutions are proposed:

$$\begin{aligned} \frac{dB_3}{dz} &= 2i\gamma A_1(0)A_2(0)e^{-i\kappa z}B_4^*, \\ \frac{dB_4^*}{dz} &= -2i\gamma A_1^*(0)A_2^*(0)e^{i\kappa z}B_3, \end{aligned} \tag{2.21}$$

where $\kappa = \beta_1 + \beta_2 - \beta_3 - \beta_4 + \gamma(P_1 + P_2)$. Differentianting B_3 twice and eliminating B_4^* yields:

$$\frac{d^2B_3}{dz^2} + i\kappa\frac{dB_3}{dz} - (4\gamma^2 P_1 P_2)B_3 = 0, \tag{2.22}$$

a similar equation is obtained for B_4^*, Thus, the solutions are:

$$\begin{aligned} B_3(z) &= (a_3e^{gz} + b_3e^{-gz})e^{-i\kappa z/2}, \\ B_4(z) &= (a_4e^{gz} + b_4e^{-gz})e^{\kappa z/2}, \end{aligned} \tag{2.23}$$

where a_3,a_4,b_3,b_4 are determined by boundary conditions, and $g = \sqrt{(\gamma P_o\rho)^2 - (\kappa/2)^2}$ is the parametric gain. The fields generated are usually labeled as signal and idler.

2.4 Cross-Polarized

To generate Cross-Polarized Spontaneous Four-Wave Mixing (XP-SFWM), the presence of birefringence in the fiber is essential. Birefringence alters the way light interacts with the media, resulting in photon pairs with a polarization different from that of the pump. This section details the incorporation of this parameter into the analysis. Furthermore, a quantum framework study is presented to obtain a crucial parameter known as the Joint Spectral Intensity, providing insights into frequency correlations.

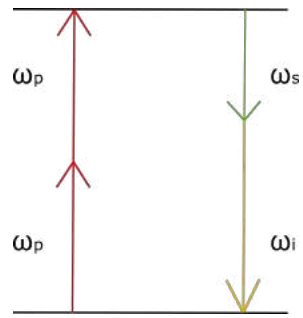

Figure 2.2: Energy diagram of the degenerated FWM

Taking birefringence into consideration in the phase matching can be accomplished by expressing the β terms in terms of the effective refractive indices:

$$\beta_j = \frac{n_j \omega_j}{c},$$

with $j = 1, 2, 3, 4$, and ensuring perfect phase matching as in the original condition,

$$\frac{1}{c}(n_1\omega_1 + n_2\omega_2 - n_3\omega_3 - n_4\omega_4) - \gamma(P_1 + P_2) = 0,$$

and by defining a secondary refractive index in which changes in the refractive index are represented as $n_i' = n_i + \Delta n_i$, it can derive the effective phase matching as follows:

$$\begin{aligned}\kappa = \frac{1}{c}(n_1\omega_1 + n_2\omega_2 - n_3\omega_3 - n_4\omega_4) + \frac{1}{c}(\Delta n_1\omega_1 + \Delta n_2\omega_2 - \Delta n_3\omega_3 - \Delta n_4\omega_4), \\ -\gamma(P_1 + P_2).\end{aligned} \tag{2.24}$$

The refractive index exhibits variations depending on the orientation of light. The impact of birefringence becomes evident when observing the difference in refractive indices along these two orientations:

$$\delta n = \Delta n_x - \Delta n_y.$$

In the scenario where the two pump waves travel along the same axis with a refractive index difference of Δn_x, while the signal and idler propagate along another axis with a difference of Δn_y, the component of the phase-matching with the refractive index difference is expressed as [22]

$$\frac{1}{c}[\Delta n_y(\omega_3+\omega_4)-2\Delta n_x\omega_1)] = \frac{1}{c}[\Delta n_y(2\omega_1)-2\Delta n_x\omega_1)]$$
$$= -\frac{2\omega_1}{c}(\Delta n_x - \Delta n_y) = -\frac{2\omega_1\delta n}{c}.$$

With this reduced birefringence term, and when considering degenerate pump conditions, the phase matching condition can be expressed as follows [20]:

$$\kappa = \frac{1}{c}(2n_1\omega_1 - n_3\omega_3 - n_4\omega_4) - 2\frac{\omega_1\delta n}{c} - 2\gamma P_1. \tag{2.25}$$

The condition of ideal phase-matching ($\kappa = 0$) and the conservation of energy are employed to identify the permissible frequencies (wavelengths) that satisfy both criteria.

In photonic applications, understanding the state of the photons being utilized is crucial. To ascertain the state of the generated photon pairs, it is essential to analyze the process of four-wave mixing through the lens of quantum optics. The initial step involves deriving the Hamiltonian of the process, which is given by:

$$\hat{H} = \hat{H}_0 + \hat{H}_{int}, \tag{2.26}$$

where the Hamiltonian of the medium can be described by two possible transitions, each corresponding to the frequencies of the signal and idler:

$$\hat{H}_0 = \hbar[\omega_s(\hat{a}_s^\dagger\hat{a}_s + 1/2) + \omega_i(\hat{a}_i^\dagger\hat{a}_i + 1/2)]. \tag{2.27}$$

And the interaction Hamiltonian is given by:

$$\hat{H}_{int} = \int_V \hat{U} dV. \tag{2.28}$$

Where V is the volume in witch the FWM occurs, and U is the is the energy density given by [34]:

$$\hat{U} = \epsilon_0\chi^{(3)}\hat{E}_{p_1}\hat{E}_{p_2}\hat{E}_s\hat{E}_i, \tag{2.29}$$

where the pump fields (E_{p_1}, E_{p_2}) are considered as monochromatic Gaussian beams. In the degenerate case, these are equal ($E_{p_1} = E_{p_2} = E_p$) and have the following form:

$$\hat{E}_p = \frac{\hat{E}_{p_0}}{2}e^{-\omega^2/2\sigma^2}\left(e^{-i[(\Omega_p+\omega)t-(k_p-\gamma P_p)z]} + e^{i[(\Omega_p+\omega)t-(k_p-\gamma P_p)z]}\right)s(\vec{r}), \tag{2.30}$$

where $s(\vec{r})$ is the normalization factor, σ is the Full-Width at Half Maximum, Ω_p is central frequency of the pump ,and E_{p_0} is the vector with the magnitude and direction of the wave. The fields of the two generated photons are quantum fields described by the annihilation and creation operators [35]:

$$\hat{E}_l = \sqrt{\frac{\omega_l\hbar}{2\epsilon_l}}\frac{1}{\sqrt{\mathcal{L}^3}}\sum_{k_l}\left(\hat{a}_l^\dagger e^{-ik_lz} + \hat{a}_l e^{ik_lz}\right)s_l(\vec{r}), \quad l = s, i \tag{2.31}$$

where $\hat{a}_l$ is the annihilation operator, $\hat{a}_l^\dagger$ is the creation operator, $\mathcal{L}^3$ is the quantized volume, and ϵ_l is the electric susceptibility at the frequency ω_l of the field. Substituting

the field in Equation 2.29 and considering the case where the pump, the signal, and the idler are co-propagating, the energy density is:

$$\hat{U} = \frac{\epsilon_0 \chi^{(3)} \hbar}{8\mathcal{L}} \sqrt{\frac{\omega_s \omega_i}{\epsilon_s \epsilon_i}} e^{-\omega^2/\sigma^2} \sum_{k_s,k_i} [\hat{a}_s^\dagger \hat{a}_i^\dagger e^{-i[2(\Omega_p+\omega_p)t-(2k_p-k_i-k_s-2\gamma P_p)z]} + \hat{a}_s \hat{a}_i e^{i[2(\Omega_p+\omega_p)t-(2k_p-k_i-k_s-2\gamma P_p)z]}] s_p^2(\vec{r}) s_s(\vec{r}) s_i(\vec{r}). \tag{2.32}$$

To account for birefringence, the equations can be written similarly to what was previously shown. Grouping the terms, we have

$$\hat{U} = S e^{-\omega^2/\sigma^2} \sum_{k_s,k_i} [\hat{a}_s^\dagger \hat{a}_i^\dagger e^{-i[2(\Omega_p+\omega_p)t-\kappa z]} + \hat{a}_s \hat{a}_i e^{i[2(\Omega_p+\omega_p)t-\kappa z]}] s_p^2(\vec{r}) s_s(\vec{r}) s_i(\vec{r}),$$

where $S = \frac{\epsilon_0 \chi^{(3)}}{8} \sqrt{\frac{\omega_s \omega_i}{(\epsilon_s+\Delta\epsilon_s)(\epsilon_i+\Delta\epsilon_i)}} \approx \frac{\epsilon_0 \chi^{(3)}}{8} \sqrt{\frac{\omega_s \omega_i}{\epsilon_s \epsilon_i}}$ if $\Delta\epsilon_l \ll \epsilon_l$ represents the gain factor, and $\kappa = 2k_p - k_i - k_s - 2\delta n \frac{k_p}{n} - 2\gamma P_p$ the phase matching condition. Due to the symmetry of the fiber, cylindrical coordinates are more suitable. The Hamiltonian of interaction is as follows:

$$\hat{H}_{int} = \frac{S\hbar}{\mathcal{L}^3} e^{-\omega^2/\sigma^2} \sum_{k_s,k_i} \int_0^r \int_0^{2\pi} \int_{-L/2}^{L/2} [\hat{a}_s^\dagger \hat{a}_i^\dagger e^{-i[2(\Omega_p+\omega_p)t-\kappa z]} + \hat{a}_s \hat{a}_i e^{i[2(\Omega_p+\omega_p)t-\kappa z]}] s_p^2(\vec{r}) s_s(\vec{r}) s_i(\vec{r}) r dr d\theta dz. \tag{2.33}$$

Defining $I = \iint s_p^2(\vec{r}) s_s(\vec{r}) s_i(\vec{r}) r dr d\theta$ as the normalization factor. Integrating over the z coordinate:

$$\int_{-L/2}^{L/2} e^{i\kappa z} dz = \frac{e^{i\kappa z}}{i\kappa}\Big|_{-L/2}^{L/2} = \frac{e^{i\kappa L/2} - e^{-i\kappa L/2}}{i\kappa} = \frac{2}{\kappa} \frac{e^{i\kappa L/2} - e^{-i\kappa L/2}}{2i}$$

$$= \frac{2}{\kappa} \sin\left(\frac{\kappa L}{2}\right) \frac{L}{L} = L \frac{\sin\left(\frac{\kappa L}{2}\right)}{\kappa L/2} = L \mathrm{sinc}\left(\frac{\kappa L}{2}\right). \tag{2.34}$$

The hamiltonian then can be written as:

$$\hat{H}_{int} = \frac{SI\hbar}{\mathcal{L}} e^{-\omega^2/\sigma^2} \sum_{k_s,k_i} \left[\hat{a}_s^\dagger \hat{a}_i^\dagger e^{-2i(\Omega_p+\omega_p)t} L \mathrm{sinc}\left(\frac{\kappa L}{2}\right) + h.c.\right]. \tag{2.35}$$

With the two components of the Hamiltonian of the system, we can employ the Heisenberg equation to determine the temporal evolution of an operator:

$$\frac{d\hat{A}}{dt} = -\frac{i}{\hbar}[\hat{A}, \hat{H}].$$

This is use to calculate the evolution of the creation operator, allowing to predict the behavior of the photons generated in the signal and idler. In this case, the Heisenberg equation for the creation operator of the signal is as follows:

$$\frac{d\hat{a}_s^\dagger}{dt} = -\frac{i}{\hbar}[\hat{a}_s^\dagger, \hat{H}] = -\frac{i}{\hbar}[\hat{a}_s^\dagger, \hat{H}_0 + \hat{H}_{int}] = -\frac{i}{\hbar}\left([\hat{a}_s^\dagger, \hat{H}_0] + [\hat{a}_s^\dagger, H_{int}]\right), \tag{2.36}$$

working on the first term:

$$
\begin{aligned}
&[\hat{a}_s^\dagger, \hat{H}_0] = [\hat{a}_s^\dagger, \hbar[\omega_s(\hat{a}_s^\dagger\hat{a}_s + 1/2)] + \omega_i(\hat{a}_i^\dagger\hat{a}_i + 1/2)] \\
&= \hbar(\omega_s[\hat{a}_s^\dagger, \hat{a}_s^\dagger\hat{a}_s + 1/2] + \omega_i[\hat{a}_s^\dagger, \hat{a}_i^\dagger\hat{a}_i + 1/2]) \\
&= \hbar\omega_s([\hat{a}_s^\dagger, \hat{a}_s^\dagger\hat{a}_s] + [\hat{a}_s^\dagger, 1/2]) + \hbar\omega_i([\hat{a}_s^\dagger, \hat{a}_i^\dagger\hat{a}_i] + [\hat{a}_s^\dagger, 1/2]) \\
&= \hbar\omega_s[\hat{a}_s^\dagger, \hat{a}_s^\dagger\hat{a}_s] + \hbar\omega_i[\hat{a}_s^\dagger, \hat{a}_i^\dagger\hat{a}_i] \\
&= \hbar\omega_s(\hat{a}_s^\dagger\hat{a}_s^\dagger\hat{a}_s - \hat{a}_s^\dagger\hat{a}_s\hat{a}_s^\dagger) + \hbar\omega_i(\hat{a}_s^\dagger\hat{a}_i^\dagger\hat{a}_i - \hat{a}_i^\dagger\hat{a}_i\hat{a}_s^\dagger) \\
&= \hbar\omega_s(\hat{a}_s^\dagger\hat{a}_s^\dagger\hat{a}_s - \hat{a}_s^\dagger\hat{a}_s\hat{a}_s^\dagger) + \hbar\omega_i(\hat{a}_s^\dagger\hat{a}_i^\dagger\hat{a}_i - \hat{a}_s^\dagger\hat{a}_i^\dagger\hat{a}_i) \\
&= \hbar\omega_s(\hat{a}_s^\dagger\hat{a}_s^\dagger\hat{a}_s - \hat{a}_s^\dagger(\hat{a}_s^\dagger\hat{a}_s + 1))
\end{aligned}
$$

$$
[\hat{a}_s^\dagger, \hat{H}_0] = \hbar\omega_s\hat{a}_s^\dagger, \tag{2.37}
$$

Similarly for the second term:

$$
[\hat{a}_s^\dagger, \hat{H}_{int}] = \frac{SI\hbar}{\mathcal{L}} e^{-\omega^2/\sigma^2} \sum_{k_s,k_i} L\text{sinc}\left(\frac{\kappa L}{2}\right) ([\hat{a}_s^\dagger, a_s^\dagger\hat{a}_i^\dagger]e^{-2i(\Omega_p+\omega_p)t} + [\hat{a}_s^\dagger, \hat{a}_s\hat{a}_i]e^{2i(\Omega_p+\omega_p)t}), \tag{2.38}
$$

where $sinc(x) = sin(x)/x$. On evaluating the commutators one gets:

$$
[\hat{a}_s^\dagger, \hat{a}_s^\dagger\hat{a}_i^\dagger] = \hat{a}_s^\dagger\hat{a}_s^\dagger\hat{a}_i^\dagger - \hat{a}_s^\dagger\hat{a}_i^\dagger\hat{a}_s^\dagger = \hat{a}_s^\dagger\hat{a}_s^\dagger\hat{a}_i^\dagger - \hat{a}_s^\dagger\hat{a}_s^\dagger\hat{a}_i^\dagger = 0,
$$

$$
[\hat{a}_s^\dagger, \hat{a}_s\hat{a}_i] = \hat{a}_s^\dagger\hat{a}_s\hat{a}_i - \hat{a}_s\hat{a}_i\hat{a}_s^\dagger = \hat{a}_s^\dagger\hat{a}_s\hat{a}_i - \hat{a}_s\hat{a}_s^\dagger\hat{a}_i = (1 - \hat{a}_s\hat{a}_s^\dagger)\hat{a}_i - \hat{a}_s\hat{a}_s^\dagger\hat{a}_i = \hat{a}_i,
$$

Applying these commutation relations to the commutator of the creation operator and the interaction Hamiltonian:

$$
[\hat{a}_s^\dagger, \hat{H}_{int}] = \frac{SI\hbar}{\mathcal{L}} e^{-\omega_p^2/\sigma^2} \sum_{k_s,k_i} \hat{a}_i e^{2i(\Omega_p+\omega_p)t} L\text{sinc}\left(\frac{\kappa L}{2}\right). \tag{2.39}
$$

with the commutators of both Hamiltonians, the Heisenberg equation (2.36) takes the form:

$$
\frac{d\hat{a}_s^\dagger}{dt} = -i\left(\omega_s\hat{a}_s^\dagger + \frac{SI}{\mathcal{L}} e^{-\omega_p^2/\sigma^2} \sum_{k_s,k_i} \hat{a}_i e^{2i(\Omega_p+\omega_p)t} L\text{sinc}\left(\frac{\kappa L}{2}\right)\right). \tag{2.40}
$$

Solving this equation as times tends to infinity [34]:

$$
\hat{a}_s^\dagger(\infty) = \hat{a}_s^\dagger(0) - i\frac{SIL}{2\sqrt{\mathcal{L}}}\frac{\sqrt{\pi}}{\sigma} \sum_{k_i} e^{-\frac{[\Delta\omega_{k_s}+\Delta\omega_{k_i}]^2\sigma^2}{4\sigma^2}} \hat{a}_i(0)\text{sinc}\left(\frac{\kappa L}{2}\right). \tag{2.41}
$$

The same procedure can be done to the creation operator for the idle. With this two operators applied to some state and in the limit when the summations became integrals [12]:

$$
|\psi\rangle = |0\rangle_s |0\rangle_i + s \iint F(\omega_s, \omega_i) |\omega_s\rangle |\omega_i\rangle d\omega_s d\omega_i, \tag{2.42}
$$

where s is the generation efficiency, and $F(\omega_s, \omega_i)$ is the Joint Spectral Amplitude (JSA), which describe the spectral entanglement properties of the photons generate, the form is [17]:

$$
F(\omega_s, \omega_i) = \alpha(\omega_s, \omega_i) \times \phi(\omega_s, \omega_i), \tag{2.43}
$$

with

$$\alpha(\omega_s, \omega_i) = e^{-\frac{(\omega_s+\omega_i-2\omega_p)^2}{4\sigma_p^2}},$$

been the pump evelope function, where $\sigma_p = \frac{\Delta\omega}{2\sqrt{2}}$ is the bandwidth, and $\Delta\omega$ is the pump spectral width. While

$$\phi(\omega_s, \omega_i) = \text{sinc}\left(\frac{\kappa L}{2}\right), \tag{2.44}$$

is the phase matching component. Usually one considers the Joint Spectral Intensity (JSI), which is the modulus square of the JSA.:

$$JSI = |F(\omega_s, \omega_i)|^2. \tag{2.45}$$

The JSI brings information of the correlation between the frequencies of the signal with the idler. The entanglement of the states can be seen in the form and orientation of the JSI, if this is close to a line with angle of 45°, it is the case where they are more correlated. On the contrary when is close to a circle, or to an irregular form, the correlations are minimal. Both cases have utility, the case where the two photons are not correlated is usually used as a source of correlated photons [36], where one of them is detected to mark the existence of the other and this is use as a single photon.

2.5 Counter-Propagation

In Counter-Propagation Spontaneous Four-Wave Mixing (CP-FWM), non-degenerate pumps are used, each directed towards one side of the optical fiber. The generated photons will share the same wavelengths as the pumps but with opposite propagation directions. This configuration is particularly interesting since phase-matching is automatically achieved in a single-mode medium such as optical fiber or a waveguide [23].

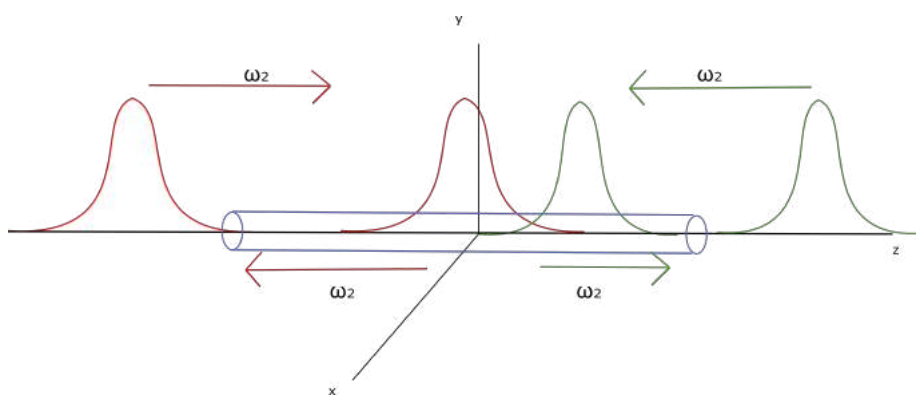

Figure 2.3: Scheme of Counter-Propagated Four Wave Mixing

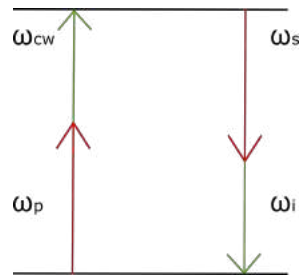

Figure 2.4: Energy diagram of the Counter-Propagated Four Wave Mixing

The quantum analysis starts in a similar way to the previous case, with the Hamiltonian:

$$\hat{H} = \frac{3}{4}\epsilon_0\chi^{(0)}\int d^3\vec{r}\hat{E}_1^{(+)}(\vec{r},t)\hat{E}_2^{(-)}(\vec{r},t)\hat{E}_1^{(-)}(\vec{r},t)\hat{E}_i^{(+)}(\vec{r},t). \tag{2.46}$$

The integration is done in the section of the fiber where the fields are temporally and spatially overlapped. The subscripts (+)/(-) refer to the positive/negative propagation direction of the electric fields. The pump fields are describe as classical fields:

$$E_\nu^{(\pm}(\vec{r},t) = A_\nu f_\nu(x,y)\int d\omega\alpha_\nu(\omega)e^{\pm i(k_\nu z-\omega t)}, \tag{2.47}$$

with $\nu = 1,2$ for the pumps fields, A_ν is the amplitude of the fields, $\alpha_\nu(\omega)$ is the spectral envelope of the pump, $f_\nu(x,y)$ is the transversal distribution of the guided mode and is normalized as $\iint |f_\nu(x,y)|^2 dxdy = 1$. The Signal and Idler fields are considered quantum fields with the form:

$$\hat{E}_\mu^{(\pm)}(\vec{r},t) = i\sqrt{\delta k}f_\mu(x,y)\sum_k e^{i(k_\mu z\mp\omega t)}l(\omega)\hat{a}_\mu^\dagger(k), \tag{2.48}$$

with $\mu = s,i$, $\delta k = 2\pi/L_Q$ is the mode spacing, L_Q is the quantization length, $\hat{a}_\mu^\dagger(k)$ the creation operator,and $l(\omega)$ is given as

$$l(\omega) = \sqrt{\frac{\hbar\omega}{\pi\epsilon_0 n^2(\omega)}}.$$

The fields are then introduced in the Hamiltonian:

$$\begin{aligned}\hat{H} = \frac{3}{4}\epsilon_0\chi^{(3)}\int d\vec{r}\left[A_1 f(x,y)\int d\omega_1\alpha_1(\omega_1)e^{i(k_1 z-\omega_1 t)}\right]\times \\ \left[A_2^* f^*(x,y)\int d\omega_2\alpha_2(\omega_2)e^{-i(k_2 z-\omega_2 t)}\right]\left[i\sqrt{\delta k}f_s^*(x,y)\sum_{k_s}e^{-i(k_s z-\omega_s t)}l(\omega_s)\right]\times \\ \left[i\sqrt{\delta k}f_i(x,y)\sum_{k_i}e^{i(k_i z-\omega_i t)}l(\omega_i)\right].\end{aligned} \tag{2.49}$$

Grouping similar terms, the Hamiltonian takes the form of:

$$\begin{aligned}\hat{H} = -\frac{3}{4}\epsilon_0\chi^{(3)}A_1A_2^*\delta k\left[\iint f_1 f_2^* f_s^* f_i dxdy\right]\sum_{k_s}\sum_{k_i}l(\omega_s)l(\omega_i) \\ \iint d\omega_1 d\omega_2\alpha_1(\omega_1)\alpha_2(\omega_2)e^{-i(\omega_1+\omega_2-\omega_s-\omega_i)t}\hat{a}_s^\dagger\hat{a}_i^\dagger\int_0^L e^{i(k_1-k_2-k_s+k_i)z}dz.\end{aligned} \tag{2.50}$$

Defining

$$f_{eff} = \iint f_1 f_2^* f_s^* f_i dxdy,$$

as the spacial overlap integral between the four fields, the phase-matching condition as $\Delta k = k_1 - k_2 - k_s + k_i$ and the difference on the frequencies $\Delta\omega = \omega_1 + \omega_2 - \omega_s - \omega_i$. And the integral with respect of z can be develop as:

$$\begin{aligned}\int_0^L e^{i\Delta kz} dz &= \frac{1}{i\Delta k} e^{i\Delta kz}\Big|_0^L = \frac{1}{i\Delta k}[e^{i\Delta kL} - 1] \\ &= \frac{2}{\Delta k} e^{i\Delta kL/2} \frac{1}{2i}\left(e^{i\Delta kL/2} - e^{-i\Delta kL/2}\right) = Le^{i\Delta kL/2} \frac{2}{\Delta kL} \sin\left(\frac{\Delta kL}{2}\right) \\ &= Le^{i\Delta kL/2} sinc\left(\frac{\Delta kL}{2}\right),\end{aligned}$$

with all this consideration the Hamiltonian take the form of

$$\begin{gathered}\hat{H} = -\frac{3}{4}\epsilon_0 \chi^{(3)} A_1 A_2^* \delta k f_{eff} L \sum_{k_s}\sum_{k_i} l(\omega_s) l(\omega_i) \\ \iint d\omega_1 d\omega_2 \alpha_1(\omega_1)\alpha_2(\omega_2) e^{-\Delta\omega t} e^{i\Delta kL/2} sinc\left(\frac{\Delta kL}{2}\right) \hat{a}_s^\dagger \hat{a}_i^\dagger\end{gathered} \tag{2.51}$$

Using the first-order perturbative method, it is possible to express the state of the generated photons as:

$$|\psi\rangle = |0\rangle_s |0\rangle_i + \frac{1}{i\hbar}\int_0^t \hat{H}(t')dt' |0\rangle_s |0\rangle_i . \tag{2.52}$$

If the time interval between the emission of the photon pair is much larger than the characteristic duration of such an event, the integral limits can be extended to

$$\int_0^t \to \int_{-\infty}^{\infty}$$

The state can be expressed as

$$\begin{gathered}|\psi\rangle = |0\rangle_s |0\rangle_i - \frac{3L}{4i\hbar}\epsilon_0 \chi^{(3)} A_1 A_2^* \delta k f_{eff} \sum_{k_s}\sum_{k_i} l(\omega_s) l(\omega_i) \\ \iint d\omega_1 d\omega_2 \alpha_1(\omega_1)\alpha_2(\omega_2) e^{i\Delta kL/2} sinc\left(\frac{\Delta kL}{2}\right) \hat{a}_s^\dagger \hat{a}_i^\dagger \int_{-\infty}^{\infty} e^{-\Delta\omega t} dt' |0\rangle_s |0\rangle_i .\end{gathered} \tag{2.53}$$

The temporal integral is related to the dirac delta with the relation:

$$\int_{-\infty}^{\infty} e^{-\Delta\omega t} dt = 2\pi\delta(\Delta\omega).$$

Using the properties of the Dirac delta, the state is:

$$\begin{gathered}|\psi\rangle = |0\rangle_s |0\rangle_i - \frac{L}{4i\hbar}\epsilon_0 \chi^{(3)} A_1 A_2^* \delta k f_{eff} \sum_{k_s}\sum_{k_i} l(\omega_s) l(\omega_i) \\ \int d\omega_1 \alpha_1(\omega_1)\alpha_2(\omega_i + \omega_s - \omega_1) e^{i\Delta kL/2} sinc\left(\frac{\Delta kL}{2}\right) \hat{a}_s^\dagger \hat{a}_i^\dagger |0\rangle_s |0\rangle_i .\end{gathered} \tag{2.54}$$

To continue the analysis, the pumps are considered Gaussian waves, and have an envelope with the form:

$$\alpha_\nu(\omega) \propto e^{-\frac{(\omega-\omega_\nu^0)^2}{\sigma_\nu^2}},$$

been ω_ν^0 the central frequency of the pump ν and σ_ν the pump bandwidth. for the scenario where one of the pumps is a continuous wave, the bandwidth tends to zero, and the Gaussian envelope tends to a Dirac delta, $\alpha_2(\omega_s+\omega_i-\omega_1) \to \delta(\omega-\omega_s-\omega_i+\omega_1)$. With these considerations, the state takes the following form:

$$\begin{aligned} |\psi\rangle = |0\rangle_s |0\rangle_i - \frac{L}{4i\hbar}\epsilon_0\chi^{(3)}A_1A_2^*\delta k f_{eff}\sum_{k_s}\sum_{k_i} l(\omega_s)l(\omega_i) \\ \alpha_1(\omega_s+\omega_i-\omega_2)e^{i\Delta kL/2}sinc\left(\frac{\Delta kL}{2}\right)\hat{a}_s^\dagger\hat{a}_i^\dagger |0\rangle_s |0\rangle_i . \end{aligned} \tag{2.55}$$

Looking at the state, it is seen that the correlation between the two frequencies is given by the elements of the envelope of the pump and the phase-matching condition, the product of those is known as the Joint Spectral Amplitude (JSA), this is define as

$$F(\omega_s,\omega_i) = \alpha_1(\omega_s+\omega_i-\omega_2)e^{i\Delta kL/2}sinc\left(\frac{\Delta kL}{2}\right). \tag{2.56}$$

And the Joint Spectal Amplitude for the Counter-Propagated FWM is

$$JSI = |F(\omega_s,\omega_i)|^2 = \alpha_1^2(\omega_s+\omega_i-\omega_2)sinc^2\left(\frac{\Delta kL}{2}\right). \tag{2.57}$$

With the JSI is possible to know the correlation between the two photons, and see if the states are in a pure state or not, the simulation of this is shown in the next chapter.

Chapter 3

Simulation

In this chapter, we present the results of the simulations based on the theoretical framework of the two cases of SFWM on fiber, in the case of the XP-SFWM a bow-tie fiber the HB800, and in the CP-SFWM a conventional telecommunication fiber the SFM-28. We start with a numerical analysis of the propagation constant, denoted as β. This analysis serves as a fundamental step in determining the phase-matching curves. Following the theoretical groundwork, we proceed to simulate both cases of FWM to obtain the JSI.

The optical fiber model employed in this study for the Cross-Polarized FWM is the HB800G, specifically designed as a polarization-maintaining fiber with a bowtie structure. The fiber's producer provides specifications including a numerical aperture (NA) of 0.18 and a core radius (r) of 4.45 μm.

In the case of the Counter-Propagated SFWM the fiber model employed was the SMF28, characterized by an 8.2 µm core diameter and a Numerical Aperture of 0.14.

3.1 Propagation constant

The initial phase involves the determination of the refractive indices for both the core and cladding of the optical fiber. To accomplish this, the Sellmeier equation for Fused Silica, as documented in [37], is employed. The specific coefficients relevant to the material are presented in Table 3.1:

	1	2	3
a_i	0.6961663	0.4079426	0.8974794
b_i (μm)	0.0684043	0.1162414	9.896161

Table 3.1: Coefficients of the Fused Silica used in this work.

The Sellmeier equation has the following form:

$$n(\lambda) = 1 + \sum_{i=1}^{3} \frac{a_i \lambda^2}{\lambda^2 - b_i^2}. \tag{3.1}$$

With the parameters of the optical fiber and Equation 2.11, the propagation constant β is calculated. By using the relationship $n_{eff} = \frac{\beta\lambda}{2\pi}$, we can determine whether the result corresponds to a mode that propagates inside the core. This is the case if $n_{cladding} < n_{effective} < n_{core}$. Figure 3.1 shows the refractive indexes of the XP-SFWM, and in Figure 3.2 the refractive indexes of the CP-SFWM are shown.

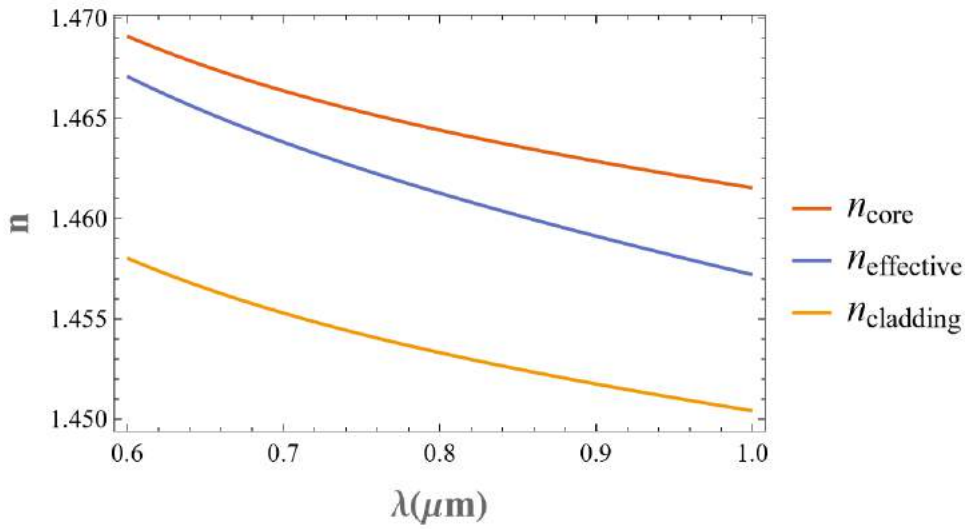

Figure 3.1: Refractive indexes of the core, cladding and the theoretical effective index of the propagated mode of the HB800.

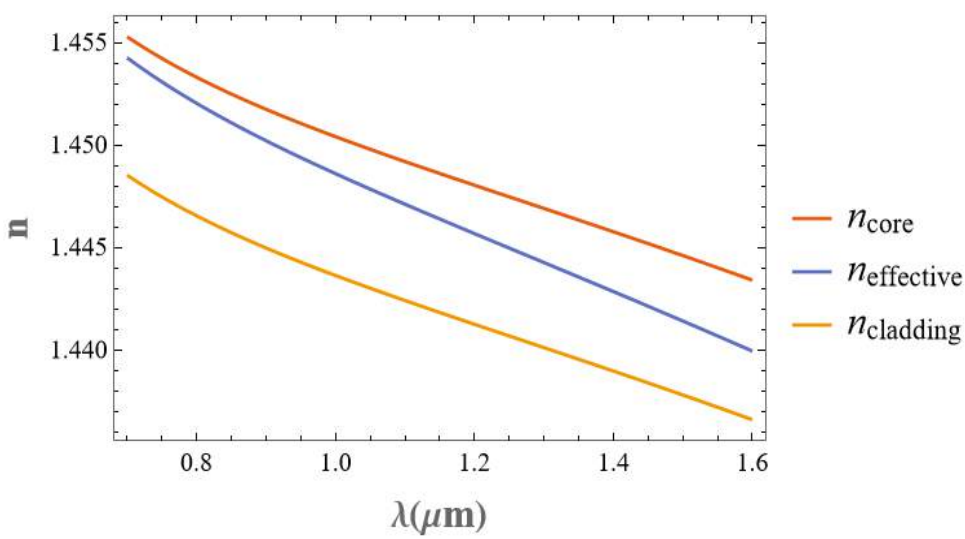

Figure 3.2: Refractive indexes of the core, cladding and the theoretical effective index of the propagated mode of the SMF28.

3.2 Cross-Polarized

To account for the effects of birefringence, an initial estimate of the difference in refractive index was obtained from Ref. [27], which suggested a value of approximately

3.7×10^{-4}. Subsequently, through a meticulous analysis of the generated photon spectra, this value was fine-tuned to approximately 3.74×10^{-4} to ensure a more accurate representation of the system's behavior.

Once the propagation constants are known, it is possible to determine the phase-matching condition using Equation 2.25. For these simulations, a pump power of 15 mW and a non-linear parameter of $\gamma = 37 \times 10^{-9}, (mW \cdot \mu m)^{-1}$ were considered. The curves depicting perfect phase matching, which were obtained using the calculated β values, are shown in Figure 3.3. With a pump wavelength of 725 nm, the signal and idler wavelengths are 628 nm and 856 nm, respectively.

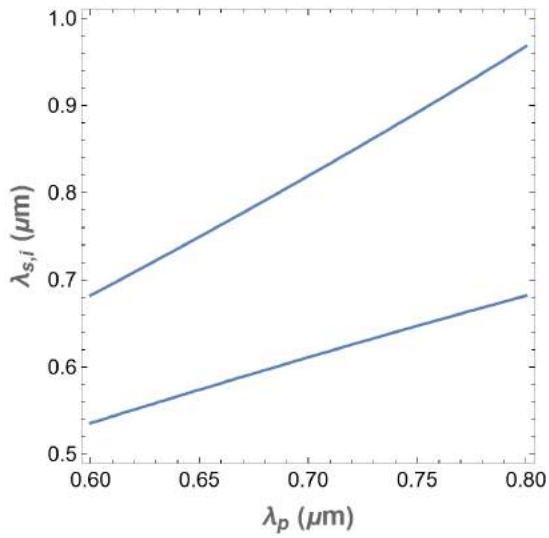

Figure 3.3: Phase matching theoretical curves for the HB800 fiber, with a range of frequency difference of 0.38-0.41 PHz in the region of interest.

With knowledge of the phase-matching condition, we can now describe the theoretical correlations between the signal and idler frequencies by simulating the Joint Spectral Intensity (JSI) and its components α and ϕ. Figure 3.4 displays both components of the JSI as well as the JSI itself, all based on a pump wavelength of 725 nm and a spectral width of 5 nm. The theoretical JSI indicates a high-frequency correlation between the two photons, this is seen by the orientation of the JSI, the structure is close to a line where a frequency of the Signal correspond to a frequency of the Idler.

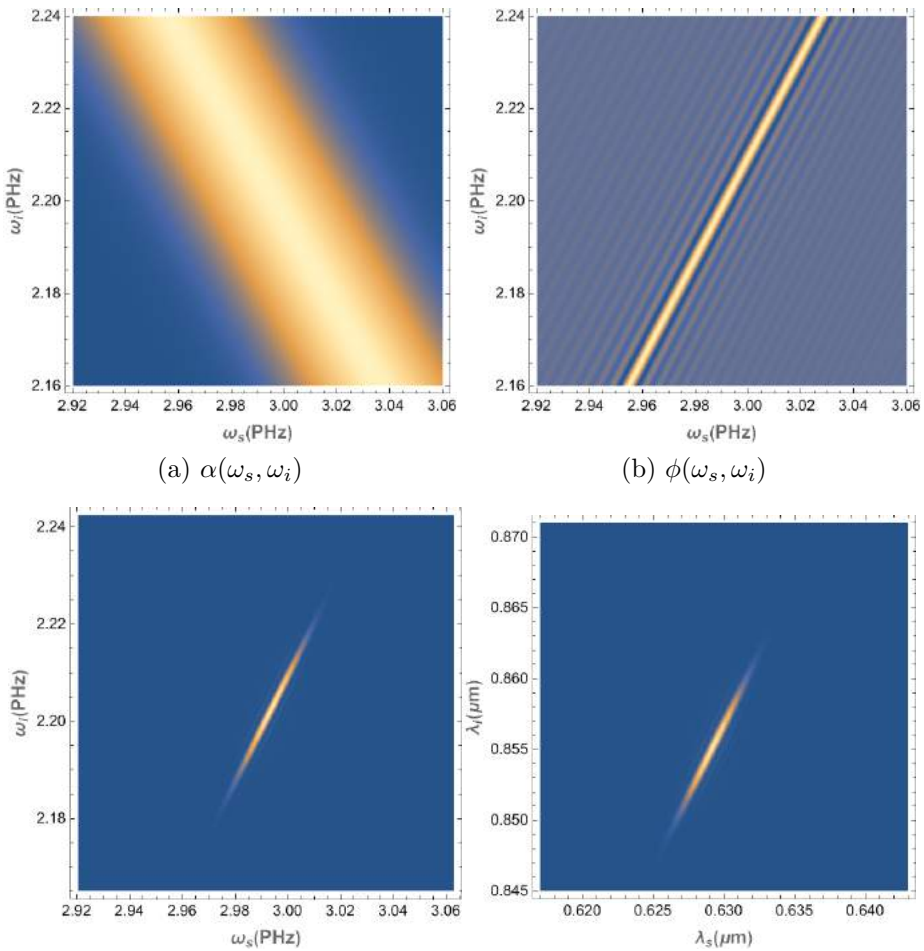

(a) $\alpha(\omega_s, \omega_i)$ (b) $\phi(\omega_s, \omega_i)$

(c) JSI(ω_s, ω_i) (d) JSI(λ_s, λ_i)

Figure 3.4: JSI and his components to the pump wavelength used in the experiment 725 nm, the (d) figure shows the JSI in terms of the wavelengths and in the range were the experimental measurements were made.

Projecting the Joint Spectral Intensity (JSI) or obtaining a marginal JSI for one of the frequencies allows us to compare the measured spectra of the generated photons. These spectra, captured with a pump wavelength of 725 nm, are depicted in Figure 3.5. In the Results section, there is a comparison between the theoretical marginal JSI and the experimentally measured spectrum.

The JSI was also calculated for various pump wavelengths, as shown in Figure 3.6. It can be seen that the JSI do not have a significant difference when changing the wavelength, in the phase-matching condition the term with more weight is the birefringence, because of this, changes in the wavelength do not alter the JSI in a significant way. Also in Figure 3.7 the marginal JSI for those wavelengths are shown.

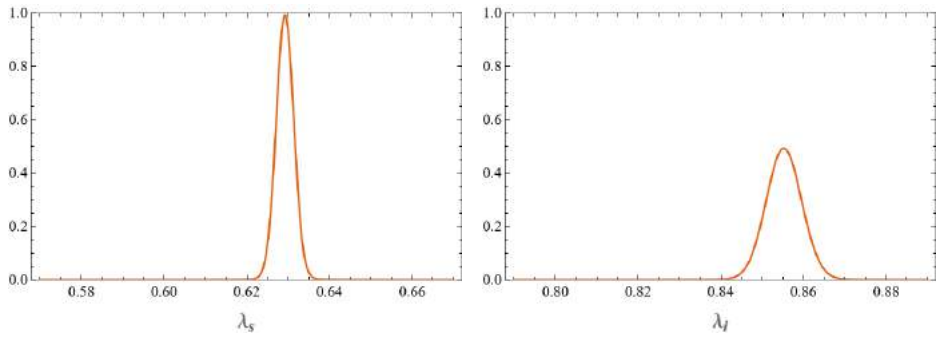

(a) Signal (b) Idlers

Figure 3.5: Theoretical spectrum of the signal and idler expected when the fiber is pump at 725 nm.

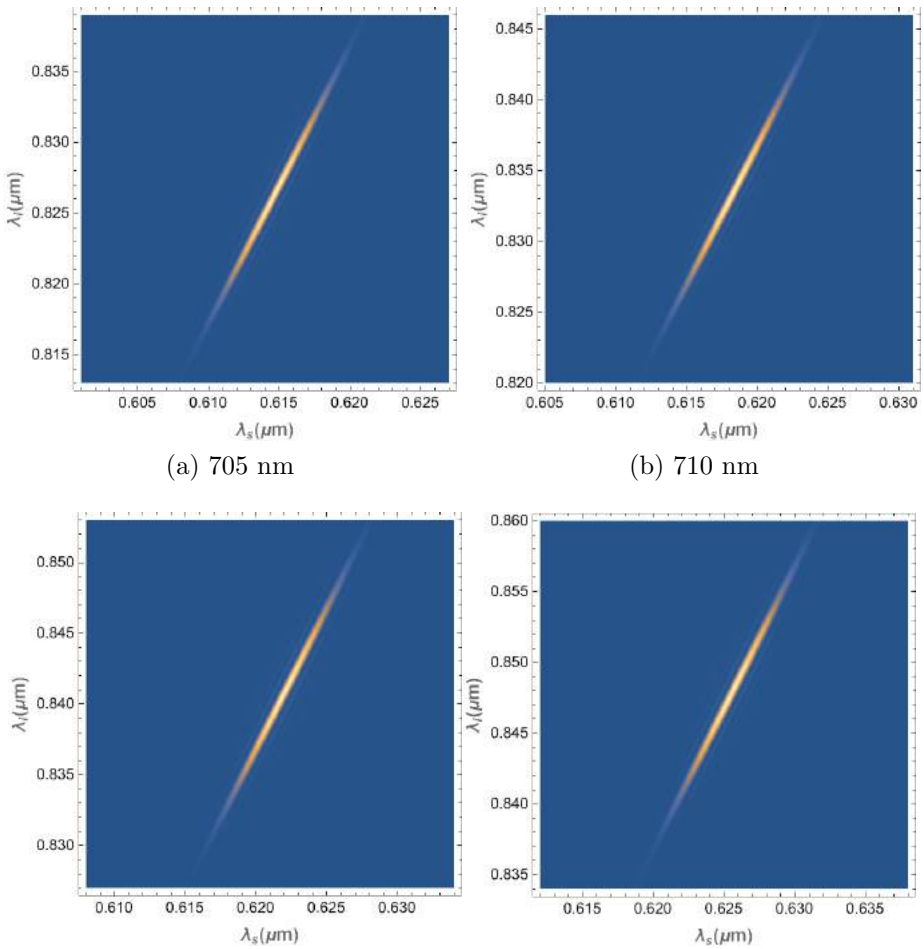

(a) 705 nm (b) 710 nm

(c) 715 nm (d) 720 nm

Figure 3.6: JSIs for different pump wavelengths.

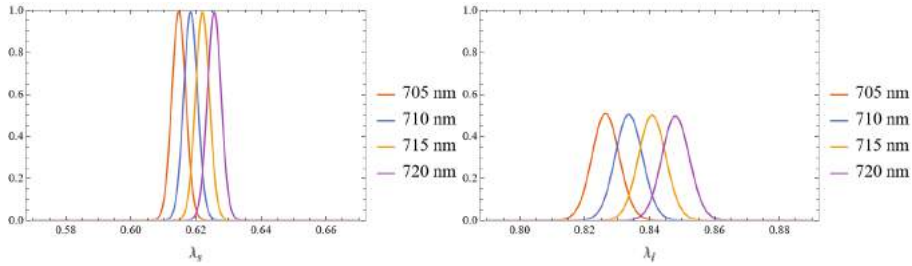

(a) Signals (b) Idlers

Figure 3.7: Theoretical spectrum of the signal and idler for different pump wavelength.

3.3 Counter-propagation

As mention for the XP-SFWM is considered a case where it can interact with the quantum memory reported in [25], where it require a photon generated at 1532 nm with a bandwidth of 150 MHz. The lasers that are considered were the Chameleon Vision II that is a tunable pulsed laser with a emission range of 680-1080 nm and the TLB-6728 Velocity, that is a CW tunable laser with a range of emission of 1520-1570 nm. The optical fiber chosen for this study was SMF28, characterized by an 8.2 µm core diameter and a Numerical Aperture of 0.14. The phase matching curves were calculated for a scenario in which the CW lasers operated at a fixed wavelength of 1532 nm, while the pulsed laser's wavelength varied.The results are depicted in Figure 3.8. It is evident from the figure that the Idler photon consistently maintains a wavelength of 1532 nm, regardless of the second laser's wavelength. Furthermore, the Signal photon exhibits the same wavelength as the varying laser.

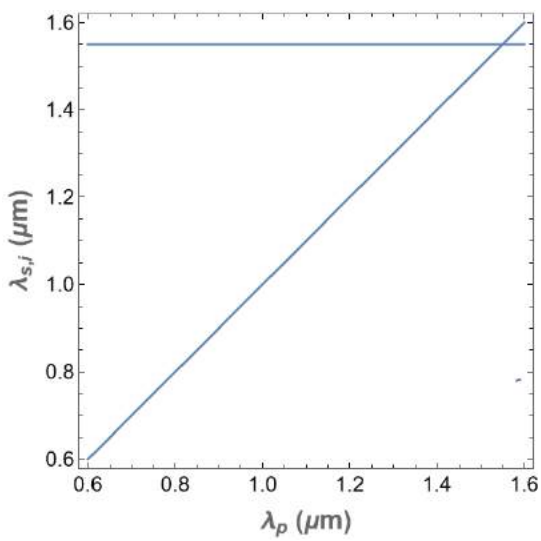

Figure 3.8: Phase-Matching for a continuum laser at 1550 nm, it can be seen that the idler will maintain the wavelength of this laser.

In Figure 3.9, the Joint Spectral Intensity (JSI) is depicted for the mixed case with a pulsed pump and a CW pump. The JSI reveals an ultra-narrow structure, primarily

oriented along the direction of the λ_i axis.

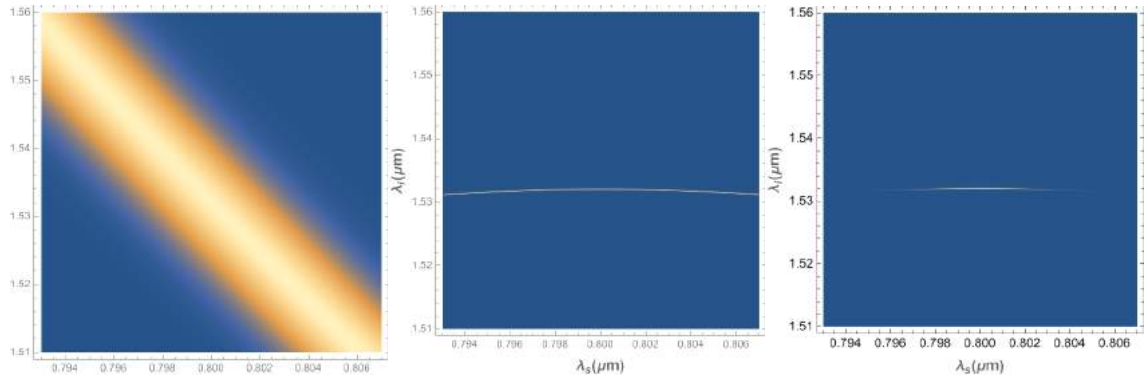

(a) α (b) ϕ (c) JSI

Figure 3.9: JSI of the counter-propagation case, it can be seeing that very narrow in comparison with the cross-polarization case.

The transition of interest have a bandwidth of 150 MHz, to predict the bandwidth that the photon will have depending on the length of the fiber it is possible to use the expression:

$$\sigma_i = \frac{2}{\sqrt{\Gamma} L(k'_p + k'_{cw}}$$

The required length of the fiber for a bandwidth of 150 MHz is 1.65 m. In Figure 3.10 the bandwidth with respect of the fiber length is represented.

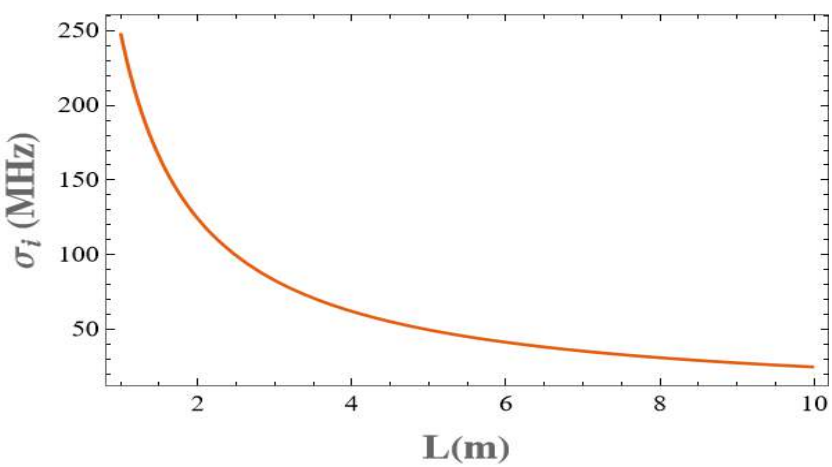

Figure 3.10: Bandwidth of the idler photon respect the fiber length.

Chapter 4

Experimental development

In this chapter the setup for generation of photon pair and correlation measurement is presented, and is utilized to measure the photons that are generated by the XP-SFWM on a bow-tie fiber model HB800. The first section will provide an overview of the entire system set up for generating the photon pair, filtering and separating the signal and idler, and measuring both spectra using the ICCD (Intensified Charge-Coupled Device) camera.

In the second section it will be present the assemble of the characterization system to measure the correlations between the two photons generated in the fiber, with the use of two monochromators and two Avalanche Photodiodes(APD).

4.1 Fiber emission

The laser employed in this study was a Coherence Chameleon Vision II, which is a pulsed and tunable Ti:Sapphire laser. It delivered a peak power of 3 W at 800 nm and offered tunability across a range from 680 nm to 1080 nm. For most of the experiments, a wavelength of 725 nm was used. All mirrors utilized in the experiment were Thorlabs broadband dielectric mirrors (BB1-E02) designed for optimal reflection in the 400-750 nm range.

The optical setup employed prior to the collection of laser light into the fiber is illustrated in Figure 4.1. The initial component utilized, in addition to the mirrors, was a Faraday Isolator (IO-5-NIR-LP). This isolator induced polarization in the non-polarized laser beam and featured a polarizing filter to prevent any reflected light from returning to the laser source.

To regulate the power within the system, a half-wave plate (model WPH05M-808 Ø1) and a polarized beam splitter (PBS102) were employed. The wave plate served to fine-tune the laser beam's polarization and adjust the power transmitted through the beam splitter, it can be seen in Figure 4.2.

In the experiment, precise control over the spectral width was crucial to tailor the form of the JSI. Narrower spectral widths were desired to produce photons with

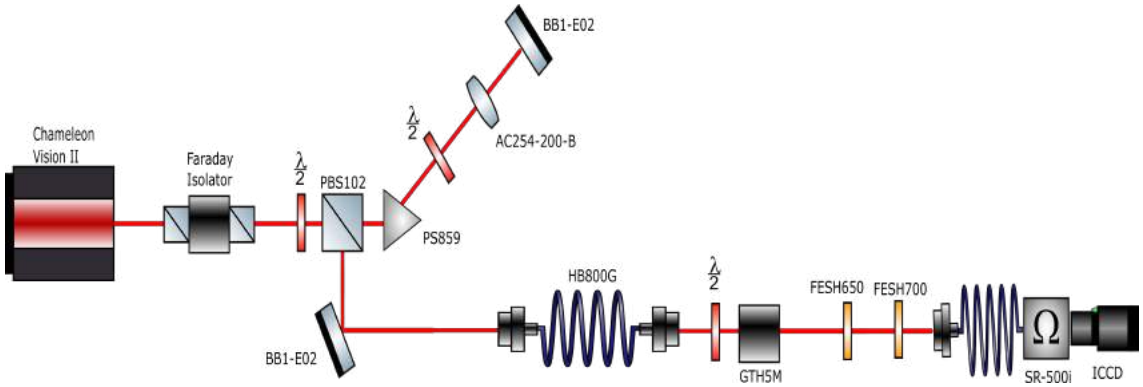

Figure 4.1: Setup to detect and measure the Signal and Idler photons, the filters before the monochromator are to measure the Signal photon, those are change for a FELH800 and a LP830 to measure the Idler photon.

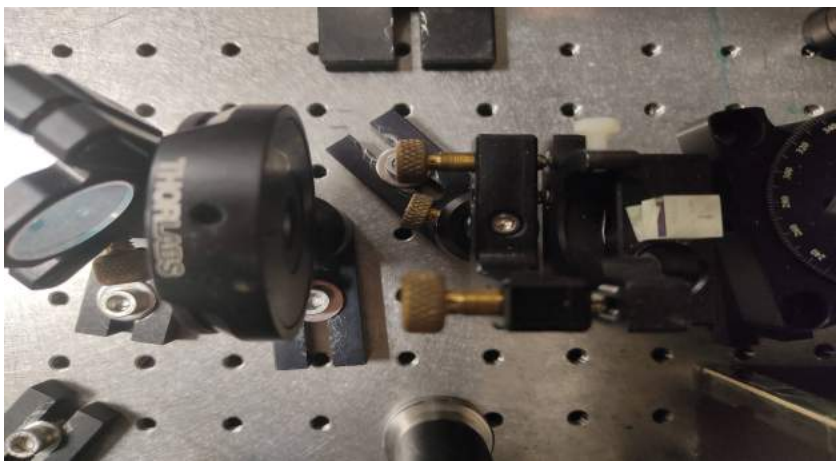

Figure 4.2: Half-Wave plate with Polarized beam splitter to control the power of the system.

factorizable states, or an entangled pair of photons with tightly defined spectra. For this work, a 5 nm spectral width was selected to generate a correlated state. To achieve this level of control, a 4f filter setup was constructed. This setup involved a lens with a 20 mm focal length (AC254-200-B), a prism (PS859), a mirror, a half-wave plate, and a frame with two razors, as it can be seen in Figure 4.3.

The focal point of the lens served as the Fourier plane, where the razors were positioned within the frame. By adjusting the frame, it was possible to control the distance between the razors, effectively cutting specific components of the light beam. Behind the razors, a mirror was placed, ensuring that the rest of the 4f setup maintained the same lens and prism used. To separate the filtered beam, a half-wave plate was introduced to induce a 45° polarization rotation. This rotation caused the beam to be reflected rather than transmitted when it reached the beam splitter.

The light reflected by the beam splitter was aligned with a mirror to ensure it followed the path leading to the HB800G fiber. For precise alignment, the mirror within

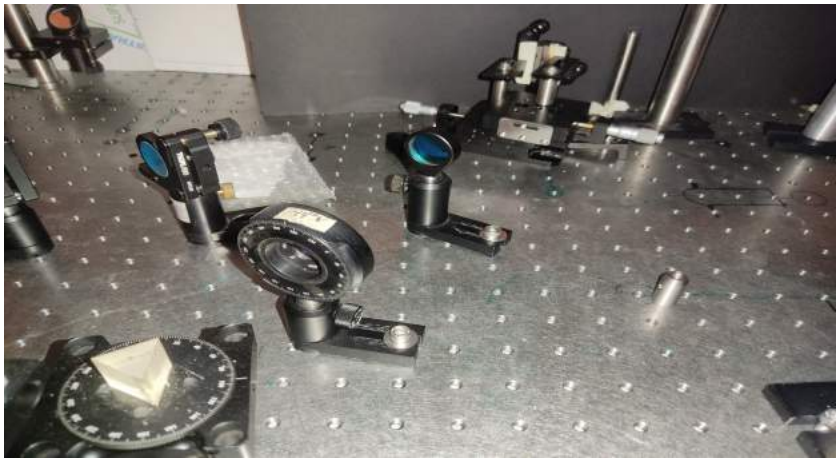

Figure 4.3: 4f filter, with a half-wave plate to rotate the polarization of the light to make it reflect in the beam splitter.

the 4f filter was used for fine-tuning. The HB800G fiber used in the experiment is a Bow-Tie Polarization-Maintaining Fiber designed for a wavelength of 830 nm, with a cut-off range of 600-800 nm, and a numerical aperture of 0.14-0.18. The specific fiber used had a length of 15 cm.

Figure 4.4: Bow-tie structure of the HB800G fiber, it was illuminated with a white light on the other face.

To orient the fiber correctly, two fiber rotators (HFR007) were employed, positioning the slow axis perpendicular to the surface of the table. Achieving the proper orientation involved using a white lamp and a CCD camera. The light illuminated the fiber, allowing the internal structure to be observed as in the Figure 4.4. The fiber rotators, along with the fiber, were mounted on multi-axis stages, this is shown in Figure 4.5.

The laser beam was coupled into the fiber using a microscope objective with a numerical aperture of 0.2 and a focal distance of 3 mm. An identical objective was placed on the other side of the fiber. The fiber was pumped with a 25 mW laser, and after optimizing the coupling, the output power was measured at 18.5 mW, representing a

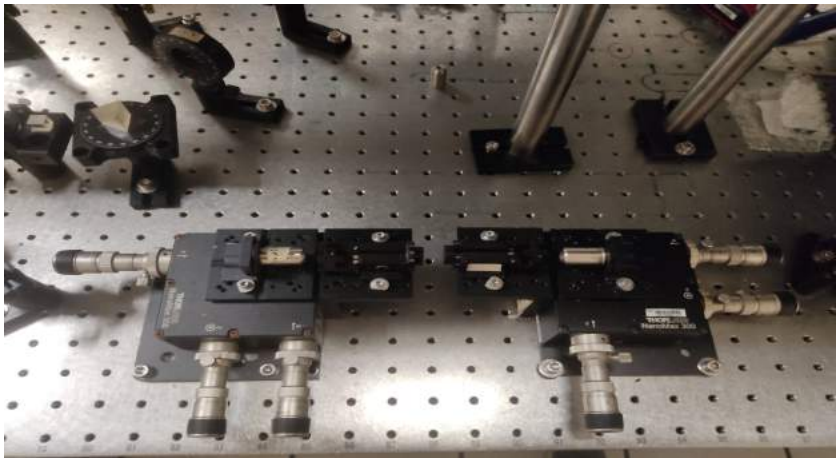

Figure 4.5: HB800G Fiber mounted in the NanoMax Stages.

collection efficiency of 74%.

Once the fiber was in place, a half-wave plate was positioned before the fiber and rotated to achieve a 45-degree rotation of polarization. Another polarized beam splitter was then introduced. A technique similar to the one reported in [20] was employed, where light travels between the two polarization axes within the fiber, creating interference upon interaction with the beam splitter. This interference results in a fringe pattern, with the spacing between the curves indicating the birefringence.
Measurements were taken using a spectrometer (CSS200) and are displayed in Figure

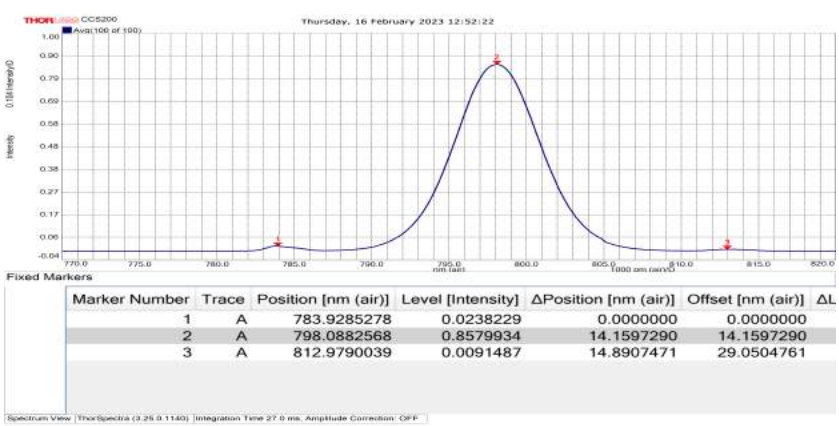

Figure 4.6: Spectrum of the laser at 800 nm, which corresponds to the optimal wavelength for the laser's operation. Additionally, two additional curves are visible, which were originally part of the laser's emission but were cut off with the 4f filter.

4.6. However, it became apparent that the spectrometer lacked the necessary resolution to fully resolve the interference structure. Consequently, the value of birefringence was obtained from the article [27], which reported a value of 3.7 ± 0.1.

The next step involved measuring the signal and idler spectrum, as these could not be observed using the spectrometer. To perform these measurements, an ICCD was used. However, before proceeding, it was essential to filter out the signal and

idler from the pump. This initial filtering process employed a half-wave plate and a Glan-Thompson Polarizer, specifically a GTH5M model. The Glan-Thompson polarizer was positioned to block light polarized horizontally, and this orientation was achieved with the assistance of a polarized beam splitter. This filter was implemented to take advantage of the fact that the signal and idler are cross-polarized to the pump wave. The filter can be seen in Figure 4.7

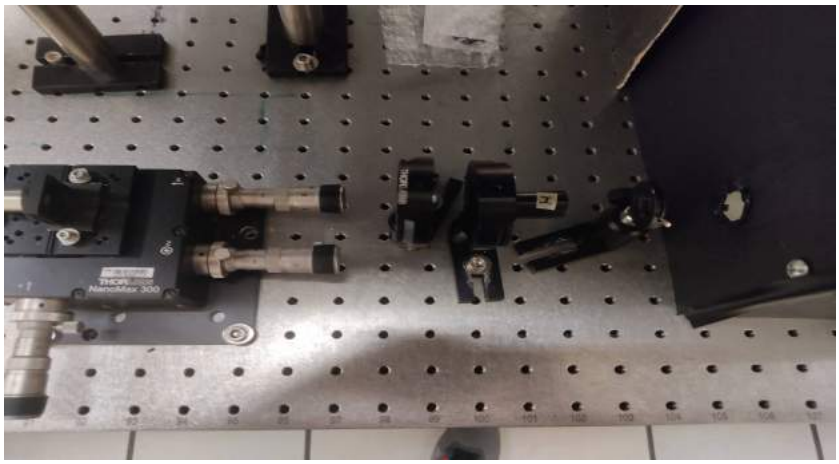

Figure 4.7: Polarization filter to extinguish the majority the pump power that transmit on the fiber.

To collect the signal and idler, a single-mode polarization maintainer fiber was employed, which was securely placed in a 3-Axis NanoMax Flexure Stage. This setup also featured a similar microscope objective to the one used with the HB800 fiber. The polarization maintainer fiber had an impressive light collection efficiency of 80%. To measure the signal and idler, various spectral filters were utilized. For the signal, the FESH700 and the FESH650 filters were used, while the idler was measured with the FELH800 and the LP830 filters, this can be seen in Figure 4.8. With the appropriate filters in place, the fiber was connected to a monochromator, specifically the Shamrock 500i model, with the ICCD camera attached to it. This setup facilitated precise spectral measurements.

The ICCD camera was used to capture the spectra of the signal and idler. The system was configured to operate in Step and Glue mode, where it recorded the photon counts within selected wavelength regions. The measurements were performed in smaller wavelength ranges of 5 nm. The ICCD camera was set with an exposure time of 5 seconds and a gain of 500. The measured spectrum of the signal and idler can be observed in Figure 4.9.

In addition to the 725 nm pump wavelength, measurements were also taken at five closely spaced wavelengths: 695 nm, 700 nm, 705 nm, 715 nm, and 735 nm. These spectrum are presented in Figure 4.10. To optimize the measurements, the exposure time was reduced to 0.5 seconds, and the system was adjusted using video mode. It's important to note that the idler was expected to have fewer counts than the signal due to the presence of additional light generated by other processes, such as Raman

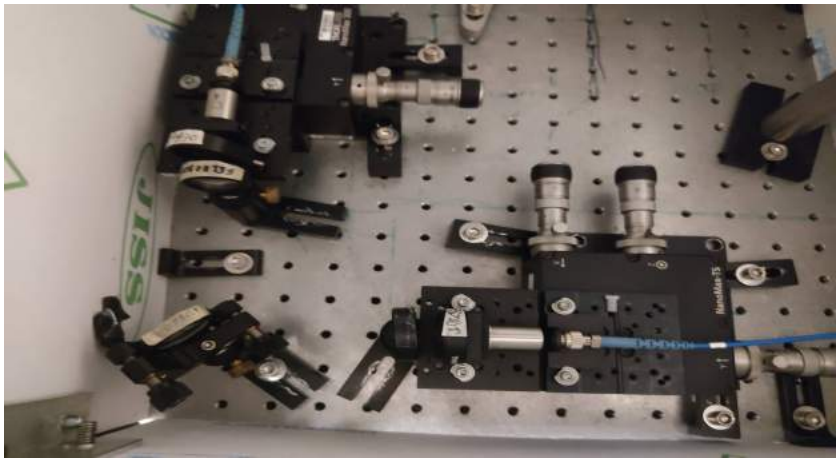

Figure 4.8: The dichroic mirror divides the Signal and Idler and both are filtered to eliminate any possible pump remaining.

scattering.

To enhance the measurement of both the Signal and Idler, two APDs (SPCM-AQRH-13-FC) and an IDQ800 were employed. A dichroic mirror (DMSP805) with a cutoff wavelength of 805 nm was used to separate the Signal and Idler. Additionally, another 3-Axis NanoMax Flexure Stage was employed, featuring a microscope objective and a fiber of the same model used in the other path. In this configuration, the Signal photons passed through the dichroic mirror (DM), while the Idler photons were reflected. The Signal path was equipped with the FESH650 and the FESH700 filters, while the Idler path featured the FELH800 and LP830 filters.

The IDQ800 is an 8-channel time-to-digital converter, coincidence counter, and time interval analyzer that receives the pulses from the APDs. The program of the IDQ800 provides the count numbers from the APDs, as well as the coincidences of the two signals. A coincidence window of 62 bins (1 bin = 81 ps) was used. The obtained counts for various pump powers at 725 nm are listed in table 4.1. The Coincidence Percentage is taken with respect to the signal counts. It is evident that the range of coincidence falls between 15-20%. To confirm that the counted photons are indeed generated by SFWM, it is expected that there should be more than 10% coincidence between the two photons.

Subsequently, coincidences were measured at other wavelengths to observe the count behavior and assess if noise from other processes was reduced. The results are presented in Table 4.2, it can be seen that usually the Idler counts are the double of the Signals, the extra counts presented in the Idler came for another processes that were generated in the infrared region, that were not possible to filter. Count optimization was achieved by fine-tuning the screws in the recollection fiber stages and adjusting the objective focus following the HB800.

Upon optimizing the coincidence counts, the fibers were reconnected to the monochromator and the ICCD. The new spectra, as shown in Figure 4.11, exhibited noticeable

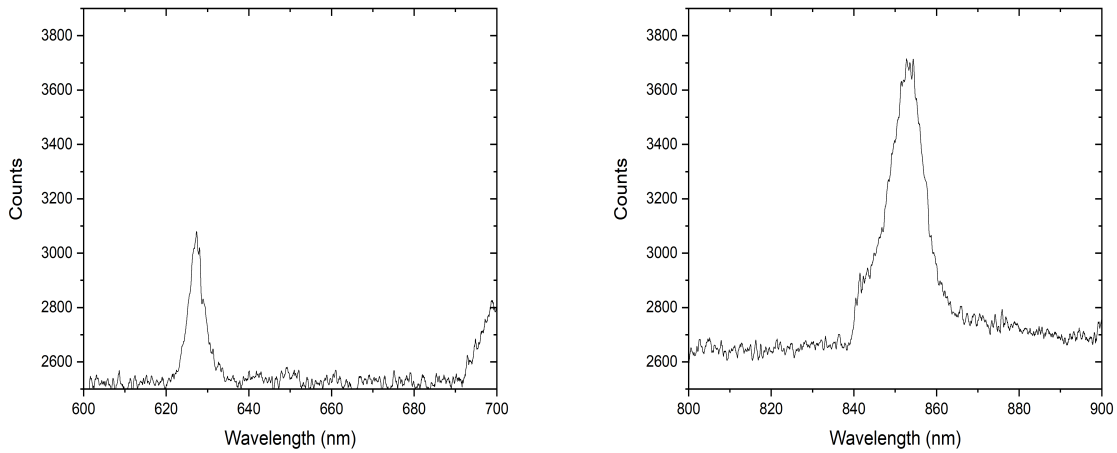

(a) Signal

(b) Idler

Figure 4.9: Counts of the Signal and Idler emission, it can be seen that contrary to the expected form for the Figure 3.5 the idler have higher counts that the signal.

Power (mW)	Counts Signal	Count Idler	Coincidence	Coincidence Percentage
10	14995	42992	2974	20%
15	37817	97145	5814	15%
20	61049	141113	9755	16%
25	98666	183316	16064	16%
30	153972	314754	27544	18%
35	242167	431072	43254	18%

Table 4.1: Coincidence table for different pump powers. As it can be seen all of the coincidence ratio is higher than 15%

differences compared to those presented in Figure 4.9. Specifically, the signal peak was taller, and the idler peak was broader.

The same procedure was done to the wavelengths that are in the Table 4.2, those can been seen in the Figure 4.12. Of this figure it is possible to see that the idler became more wider as the wavelength increase.

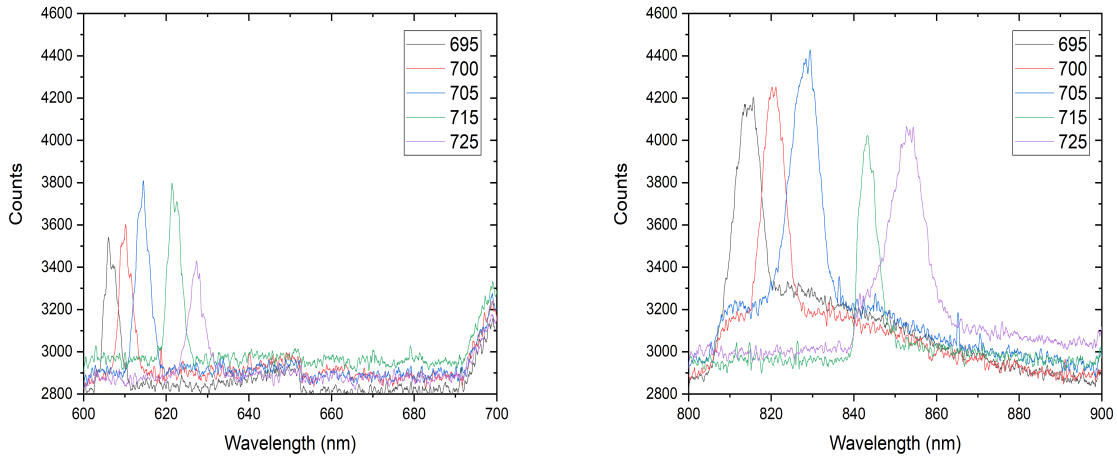

(a) Signal (b) Idler

Figure 4.10: Counts of the Signal and Idler for five different wavelengths around the central wavelength of 725 nm.

Wavelength(nm)	Counts Signal	Count Idler	Coincidence	Coincidence Percentage
705	165947	344950	30097	18%
710	156422	386545	29322	19%
715	98666	183316	16064	16%
720	167890	224557	27386	16%
730	159955	183746	25367	16%

Table 4.2: Counts at different wavelength, the pump power used was of 25 mW.

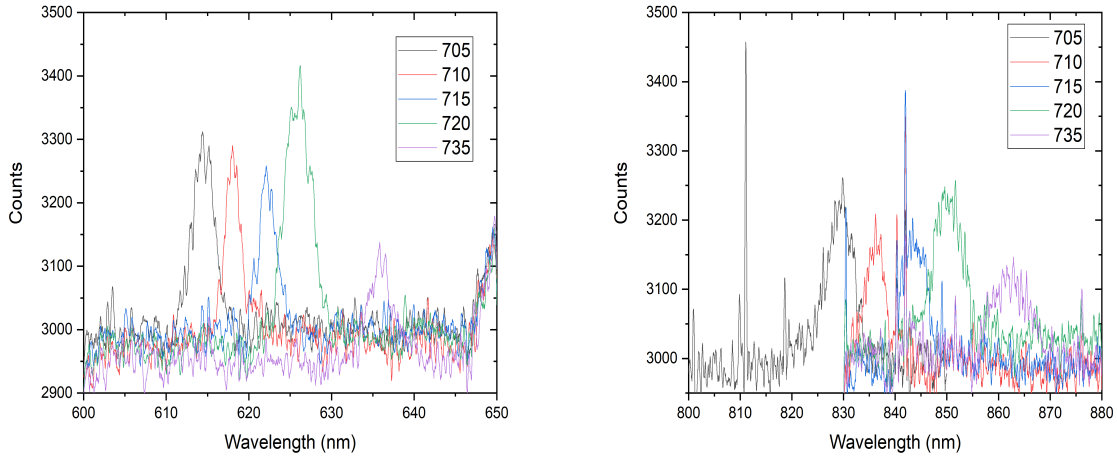

(a) Signal (b) Idler

Figure 4.12: Spectra of four different wavelengths, it can be seen that the larger pump wavelength the Idler became wider.

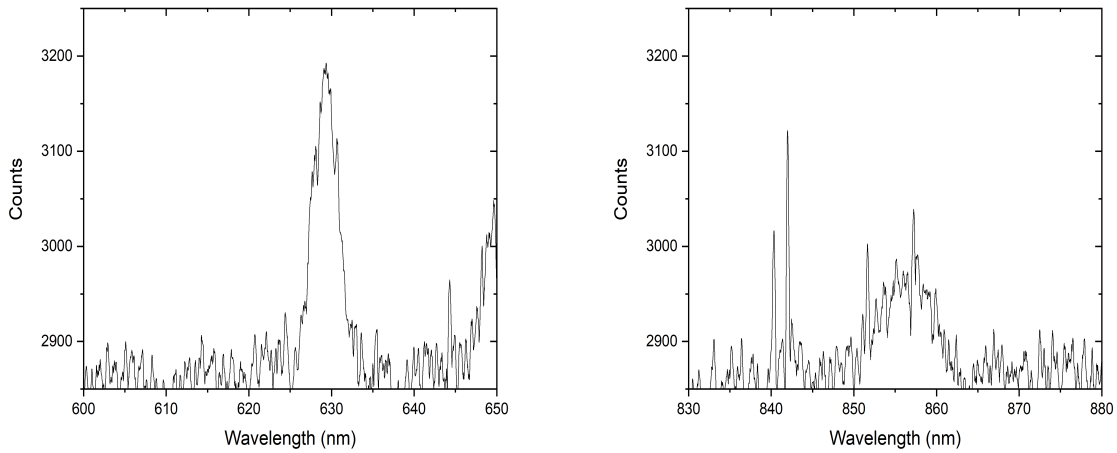

(a) Signal

(b) Idler

Figure 4.11: Spectra for Signal and Idler one the coincidence were optimized, the form of both emissions have a big difference to the seen without this optimization.

4.2 Spectral Characterization

Now that the system has optimized the coincidence of the photons generated in the FWM process, the next step is to determine the correlation relation between them, ultimately obtaining the JSI. To accomplish this objective, a dedicated characterization system was essential. This system facilitated the scanning of signal and idler wavelengths and allowed the measurement of coincidence at each point in the spectral domain. The implementation of this system hinged on the utilization of two monochromators to precisely select the wavelengths of interest, two Avalanche Photodiodes (APDs) to measure photon counts in both signal and idler paths, and the IDQ800 to quantify the amount of coincidence between these photons. The scheme of the array is show in Figure 4.13

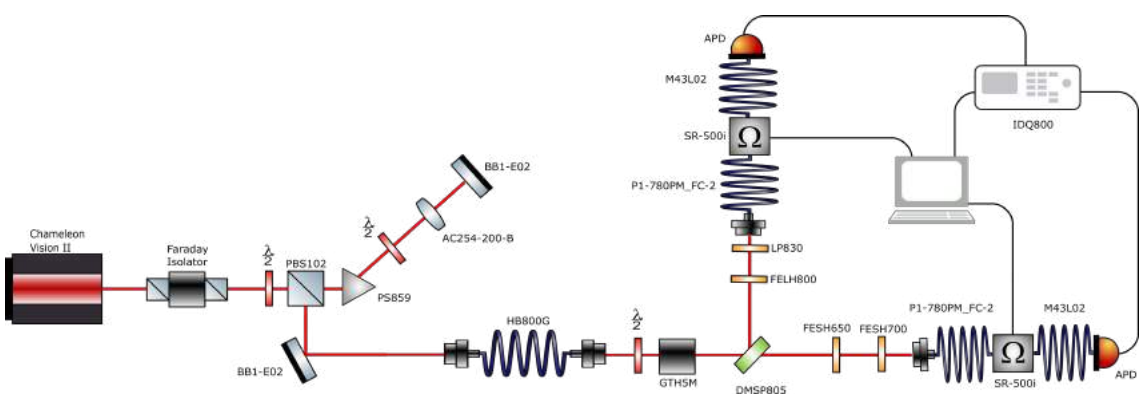

Figure 4.13: Array of the complete system of characterization, with the PC controlling the monochromators, and receiving the counts and coincidence of the IDQ800.

The initial step involved determining the efficiency of the monochromators. By removing the filters in the transmitted path, the pump light was collected and directed into the entrance of a monochromator. At the exit, a multimode fiber with a 105 μm radius was placed. The entrance fiber received 4.60±0.05 mW of collected power, while the exit fiber had 0.12 mW±0.05 and 0.13 mW±0.05 in each one, indicating a 2% efficiency for both monochromators.

Subsequently, the fibers were reconnected to the APDs, and both paths were adjusted to achieve one million counts with one second of exposure. The recollection fibers were then connected to the monochromators, and at the exit ports of both monochromators, multimode fibers were attached, connecting them to the APDs.

Figure 4.14: Monochromators withe APDs connected, the cardboard box around was needed because there was a big amount of the laser light entering the APDs.

The multimode fiber was recollecting a big amount of noise due to the light of the laser that was been dispersed with almost nine thousand extra counts, to prevent it a box was built with cardboard, reducing to just one thousands of noise with one second of exposition time. Most of the light was entering on the multimode fibers due to their jacket letting transmission window. The setup of the system is show in the Figure 4.14

With the system in these conditions, counts were measured in both paths, and the data is presented in Figure 4.15. It's evident that the signal is taller than the idler, which is wider, consistent with what is expected based on Figure 3.5.

Then measurements of coincidence were conducted to obtain the JSI. The measurement range extended from 617 nm to 643 nm for the Signal and from 845 nm to 871 nm for the Idler, with a step size of 0.5 nm. The time exposure was set to 30 seconds, and the system was controlled by a LabVIEW program. The results of these measurements are displayed in Figure 4.16. The next section will discuss all the results obtained and compare them with the theoretical expectations.

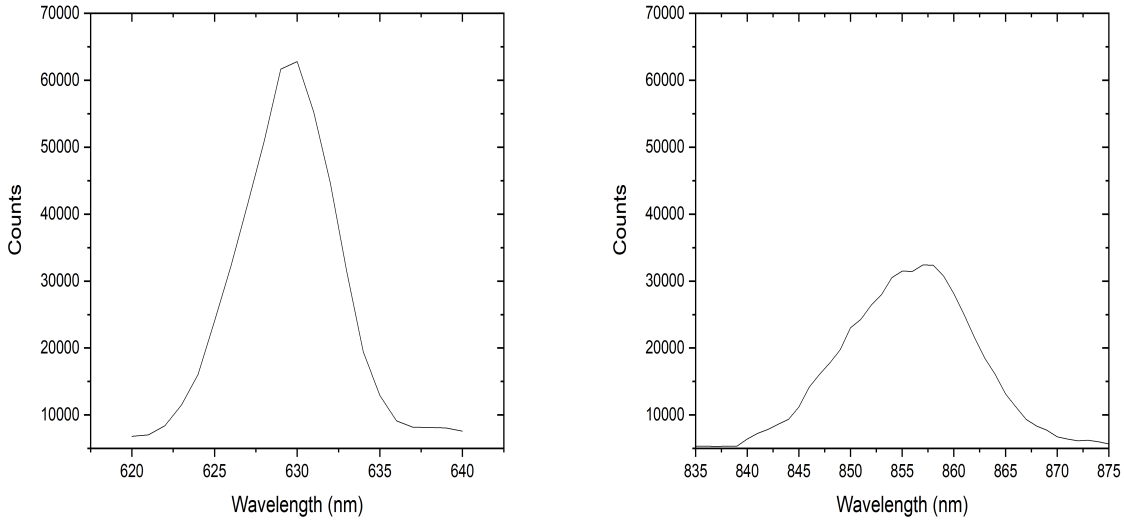

(a) Signal (b) Idler

Figure 4.15: Counts taken with the APDs step by step with the monochromator, as it can be seen have less noise to those taken with the ICCD.

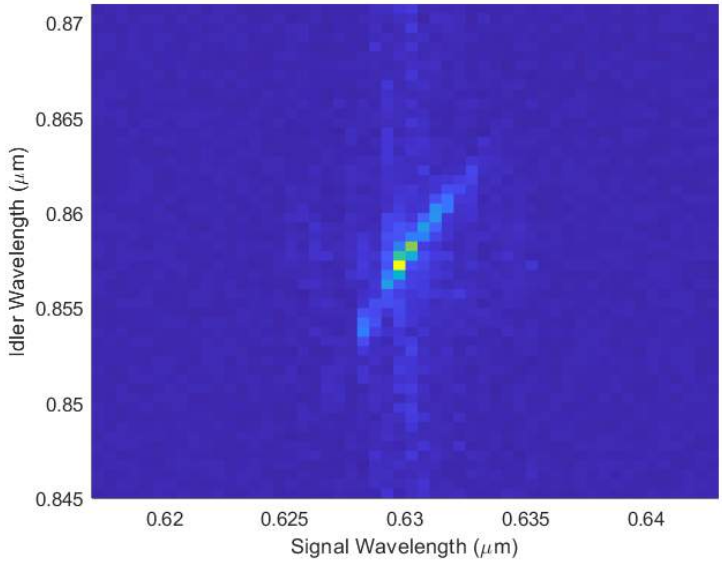

Figure 4.16: Experimental JSI obtained, it present an orientation of 56.30°.

The software program employed to control and automate the measurements was originally crafted by Hector Cruz Ramirez, a colleague from the Universidad Nacional Autonoma de Mexico. This program served as the basis and was subsequently modified to seamlessly interface with the specific models of monochromators utilized within the institution.

4.3 ICCD measurement

Another approach that was attempted involves using the ICCD camera triggering the gain when an APD detects a photon. This method still requires some improvements, and a result has not been obtained yet.

In this section, an alternative technique for measuring the coincidence of the photon pair will be presented. This method involves the use of monochromators, an APD, the ICCD, and some Phillips modules that modify electrical signals. The objective is to introduce a time delay between the signal of the arriving of the Idler photons at the APD to activate the photocathode of the ICCD when the Signal photons arrives. With this technique, it is possible to measure a full wavelength in a small amount of time compared to the technique used in the previous section.

The same setup was used up to the connection of the recollection fibers. However, for this case the fiber of the Signal path was connected to 20 meters of single-mode fiber, introducing one hundred second of delay in the arrival of the photons to the ICCD. In the Idler path the recollection fiber was connected to the APD, and the BNC cable was disconnected of the IDQ800 and connected to some Phillips modules to convert it to a TTL signal. All the modules accept negative voltage, so the first element connected was a Phillips model 760 to change the polarization of the signal. Then signal was connected to the module 704 which change the pulse to a NIM pulse, the module can change the width of the pulse with a screw. Then the signal was connected to the module 792 which is two section delay, with steps of 0.5 ns, with a total delay of 127 ns, 63.5 ns in each delay. The coaxial cables use to interconnect the modules introduce a time delay in the signal of 3.5 ns.

The output signal was connected to a BNC cable with a Phillips model 760 to transform the signal to a TTL. This cable was connected to the Direct Gate of the ICCD. For the ICCD, a coaxial cable was connected to the Gate monitor, which was then connected to an oscilloscope to monitor the activation of the photocathode. Additionally, a BNC was connected to another output of the module 704 and connected to the oscilloscope. This was done with the objective of observing the time delay presented between the NIM pulse and the photocathode activation.

The ICCD was configured to be in internal trigger with gain triggered by the direct gate. The objective was to activate the gain when the Signal photon arrives, capturing all the wavelength correlations. To achieve this, it was necessary for the Idler signal to arrive 20 ns before the Signal, which is the response time of the ICCD. The exposure time was set to 30 seconds, and the acquisition was set in video mode. The time delay was increased with the modules to find the optimal time delay, determined to be 20 ns with a width in the TTL pulse of 50 ns. The spectra taken can be seen in Figure 4.18.

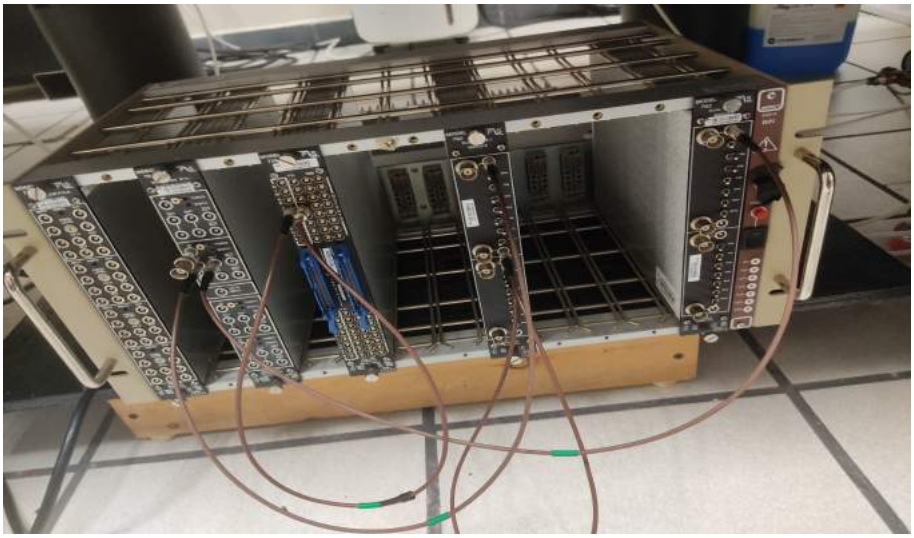

Figure 4.17: Phillips modules, with 704 726,792

As can be observed, the spectra are barely distinguishable from the noise level. This was with four hundred thousand counts in the Idler APD, just below the recommended frequency on the Photocathode of five hundred thousand. Subsequently, attempts were made to reduce the width of the TTL pulse, but even with a 40 ns width, it became exceedingly challenging to differentiate the spectra from the noise. The target width was 10 ns but achieving this within the required time frame proved to be impossible.

Figure 4.18: Spectra of the signal with a width of 50 ns, the width of the pulse determine the time window in which the gain is active.

Chapter 5

Discussion and conclusions

With all the data of the simulation and the experimental measurements, it is time to perform a comparative analysis and evaluate the effectiveness of the spectral characterization system for the XP-SFMW. As previously mentioned, the birefringence value was calibrated using the experimental data derived from the ICCD spectra. This calibration process involved determining the highest point of each curve as shown in Figure 3.3. Utilizing this adjusted birefringence data, the phase-matching curve was modified, as clearly demonstrated in Figure 5.1. There is an excellent agreement between the experimental data and the phase-matching curve.

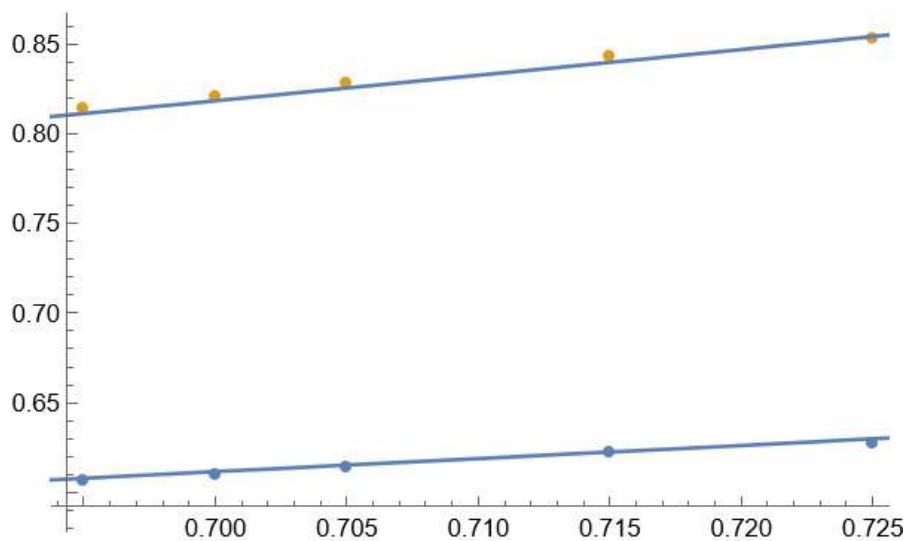

Figure 5.1: Phase-Matching curve compare to the central wavelengths measured.

The projection of the JSI over the Signal and Idler wavelengths can be directly compared with the counts obtained with the APDs and monochromators. As shown in Figure 5.2, it's worth noting that both the experimental data and the simulation were normalized based on their respective highest values to ensure a clear comparison. These curves exhibit a good agreement with the data. Once again, the central wavelength of the Idler photon exhibits a slight variation, while the width of both curves is nearly identical. This further validates the alignment between the experimental results and the simulation.

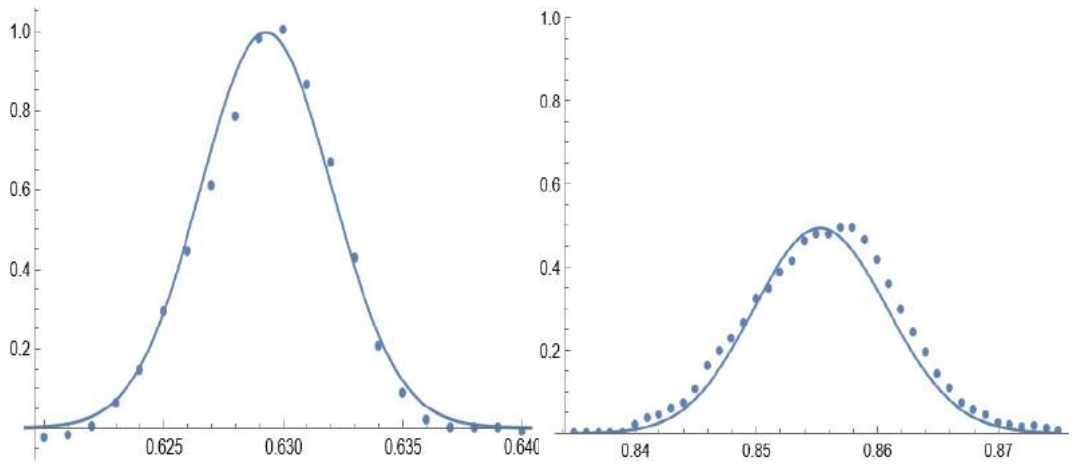

(a) Signal (b) Idler

Figure 5.2: Counts measured with the APDS, against theoretical marginals JSI.

It is evident that the model employed for simulating the fiber yields results that closely align with those obtained in the experimental measurements. This congruence between the model and the real data is a positive indication, especially for comparing the theoretical JSI with the experimental coincidence measurements and evaluating the effectiveness of the characterization system. Both aspects are illustrated side by side in Figure 5.3.

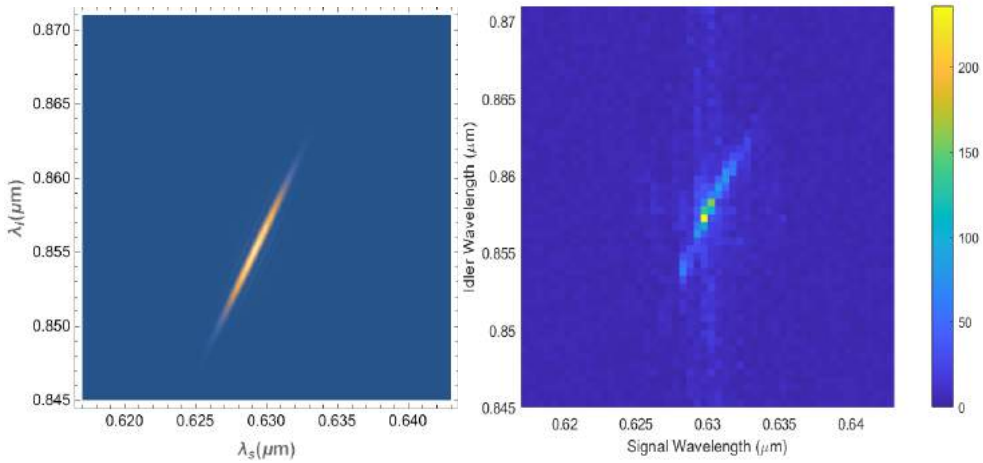

(a) Theoretical (b) Experimental

Figure 5.3: Theoretical and Experimental JSI, both were plotted in the same range for easy comparison.

The experimental measurements appear truncated in comparison to the theoretical JSI. This truncation could be attributed to an insufficient exposure time for capturing the entire coincidence structure. However, it is noteworthy that the orientation

of the coincidence pattern is akin to that observed in the experimental data. As mentioned in the experimental section, the presented orientation is approximately 56.3°±2°, whereas the theoretical orientation is approximately 51.88°. This theoretical value was determined using Equation 5.1.

$$\theta = -\arctan\left(\frac{\tau_s}{\tau_i}\right) \tag{5.1}$$

where $\tau_\mu = L[\beta'_p - \beta'_\mu]$ [19].The discrepancy between the measured JSI an the theoretical result, could be assing to the length of the fiber, that was reduced when this was cut and the amount of counts that were obtained with the exposition time used.

The characterization system has demonstrated its capability to perform accurate measurements of the correlations between Signal and Idler photons, seen that the JSI obtained is similar to the theoretical obtained. This confirmation of the system's effectiveness opens the door for its application in various other experiments as it will be the CP-SFWM, and future experiment with SPDC.

The main challenge encountered in the characterization system was the substantial losses in the monochromators. Even with a narrow spectral width of 5 nm and the pump power reduced by the 4f filter, only 4% of the power was captured. This was particularly evident in the coincidence measurements, where the peak value recorded with a 30-second exposure time was only 236.

A potential future enhancement for the system could involve replacing the monochromators with diffraction elements controlled by rotating mounts. This change could serve a dual purpose: reducing losses and creating a more compact system for easier integration into other experiments. By improving the power transmission through the characterization system, it would be possible to reduce the data acquisition time or maintain the same exposure time for more precise measurements. With appropriate characterization of the rotatory mounts, a higher resolution can be achieved, allowing for smaller measurement steps.

Regarding the ICCD measurements, there is room for improvement in the implementation of the technique. The use of two monochromators can potentially reduce the count rate, allowing for an increase in the power introduced to the fiber and, consequently, more photons in the Signal path for detection. However, additional work is needed to determine the optimal width of the TTL pulse for JSI measurements. A pulse that is too wide may introduce counts unrelated to the measurement, while a pulse that is too short may not provide sufficient counts to distinguish from noise. Exploring these alternatives and finding better solutions will be part of future research efforts.

Due to technical malfunctions with the laser, the measurement of the Joint Spectral Intensity (JSI) for the Counter-Propagating case could not be completed within the timeframe of this study. This aspect will be addressed promptly. Nonetheless, even with this component pending, this work marks the initial phase in constructing a fully integrated quantum memory. Since a quantum memory will require a factorizable photon pair state, to compare the store photon, with the other. The subsequent phase

involves implementing CP-SFWM and characterizing the photon pair spectral correlations. Once achieved, this photon pair can serve as the source for the quantum memory in an erbium-doped optical fiber, as detailed in [25].

In conclusion, in this work spectral characterization system that meets the requirements for precise measurement of photon correlations has been successfully developed (implemented and characterized). It has been demonstrated that this system provides results that closely align with theoretical expectations. This accomplishment represent the first step into the construction of a complex system of a quantum memory in erbium-doped fiber with a photon source with factorizable states generated by Counter-Polarized Spontaneous Four Wave Mixing.

Bibliography

[1] Yudong Cao, Jonathan Romero, Jonathan P. Olson, Matthias Degroote, Peter D. Johnson, Mária Kieferová, Ian D. Kivlichan, Tim Menke, Borja Peropadre, Nicolas P. D. Sawaya, Sukin Sim, Libor Veis, and Alán Aspuru-Guzik. Quantum chemistry in the age of quantum computing. *Chemical Reviews*, 119(19):10856–10915, August 2019.

[2] Nandhini S, Harpreet Singh, and Akash U N. An extensive review on quantum computers. *Advances in Engineering Software*, 174:103337, 2022.

[3] Gorjan Alagic, Anne Broadbent, Bill Fefferman, Tommaso Gagliardoni, Christian Schaffner, and Michael St. Jules. *Computational Security of Quantum Encryption*, page 47–71. Springer International Publishing, 2016.

[4] Ji-Gang Ren and the others. Ground-to-satellite quantum teleportation. *Nature*, 549(7670):70–73, August 2017.

[5] M Chen, Z; Segev. Highlighting photonics: looking into the next decade. *elight*, 1, 2021.

[6] Y. Ding, D. Llewellyn, I. I. Faruque, D. Bacco, K. Rottwitt, M. G. Thompson, J. Wang, and L. K. Oxenlowe. Quantum entanglement and teleportation based on silicon photonics. In *2020 22nd International Conference on Transparent Optical Networks (ICTON)*, pages 1–4, 2020.

[7] Wen-Zhao Liu, Yu-Zhe Zhang, Yi-Zheng Zhen, Ming-Han Li, Yang Liu, Jingyun Fan, Feihu Xu, Qiang Zhang, and Jian-Wei Pan. Toward a photonic demonstration of device-independent quantum key distribution. *Phys. Rev. Lett.*, 129:050502, Jul 2022.

[8] P. C. Miller. Optical Second Harmonic Generation in piezoelectric cystals. *Applied Physics Letters*, 5(1):17–19, 1964.

[9] D. A. Kleinman. Theory of second harmonic generation of light. *Phys. Rev.*, 128:1761–1775, Nov 1962.

[10] C. Couteau. Spontaneous parametric down-conversion. *Contemporary Physics*, 59(3):291–304, 2018.

[11] Sean M. Spillane, Marco Fiorentino, and Raymond G. Beausoleil. Spontaneous parametric down conversion in a nanophotonic waveguide. *Opt. Express*, 15(14):8770–8780, Jul 2007.

[12] K. Garay-Palmett, D. Cruz-Delgado, F. Dominguez-Serna, E. Ortiz-Ricardo, J. Monroy-Ruz, H. Cruz-Ramirez, R. Ramirez-Alarcon, and A. B. U'Ren. Photon-pair generation by intermodal spontaneous four-wave mixing in birefringent, weakly guiding optical fibers. *Phys. Rev. A*, 93:033810, Mar 2016.

[13] F. Triana-Arango, Ramos-Ortiz G, and R Ramírez-Alarcón. Spectral Considerations of Entangled Two-Photon Absorption Effects in Hong–Ou–Mandel Interference Experiments. *The Jornal of Physical Chemistry A*, 127(11):2608–2617, 2023.

[14] Francesco Graffitti, Peter Barrow, Alexander Pickston, Agata M. Brańczyk, and Alessandro Fedrizzi. Direct generation of tailored pulse-mode entanglement. *Phys. Rev. Lett.*, 124:053603, Feb 2020.

[15] B. C. Hiesmayr, M. J. A. de Dood, and W. Löffler. Observation of four-photon orbital angular momentum entanglement. *Phys. Rev. Lett.*, 116:073601, Feb 2016.

[16] Y. Chen, S. Ecker, L. Chen, F. Steinlechner, M. Huber, and R. Ursin. Temporal distinguishability in Hong-Ou-Mandel interference for harnessing high-dimensional frequency entanglement. *npj quantum information*, 7(167), Dec 2021.

[17] K. Garay-Palmett, H. J. McGuinness, Offir Cohen, J. S. Lundeen, R. Rangel-Rojo, A. B. U'Ren, M. G. Raymer, C. J. McKinstrie, S. Radic, and I. A. Walmsley. Photon pair-state preparation with tailored spectral properties by spontaneous four-wave mixing in photonic-crystal fiber. *Opt. Express*, 15(22):14870–14886, Oct 2007.

[18] R de J León-Montiel, J Svozilík, L J Salazar-Serrano, and Juan P Torres. Role of the spectral shape of quantum correlations in two-photon virtual-state spectroscopy. *New Journal of Physics*, 15(5):053023, May 2013.

[19] Karina Garay-Palmett, Dong Beom Kim, Yujie Zhang, Francisco A. Domínguez-Serna, Virginia O. Lorenz, and Alfred B. U'Ren. Fiber-based photon-pair generation: tutorial. *J. Opt. Soc. Am. B*, 40(3):469–490, Mar 2023.

[20] Brian J. Smith, P. Mahou, Offir Cohen, J. S. Lundeen, and I. A. Walmsley. Photon pair generation in birefringent optical fibers. *Opt. Express*, 17(26):23589–23602, Dec 2009.

[21] Bin Fang, Offir Cohen, Jamy B. Moreno, and Virginia O. Lorenz. State engineering of photon pairs produced through dual-pump spontaneous four-wave mixing. *Opt. Express*, 21(3):2707–2717, Feb 2013.

[22] G. P. Agrawal. *Nonlinear fiber optics*. Academic Press, 2013.

[23] Jorge Monroy-Ruz, Karina Garay-Palmett, and Alfred B U'Ren. Counter-propagating spontaneous four wave mixing: photon-pair factorability and ultra-narrowband single photons. *New Journal of Physics*, 18(10):103026, October 2016.

[24] Xue-W. He Q. et al. Jiang, MH. Quantum storage of entangled photons at telecom wavelengths in a crystal. *Nature Communications*, 14(6995), 2023.

[25] Erhan Saglamyurek, Jeongwan Jin, Varun B. Verma, Matthew D. Shaw, Francesco Marsili, Sae Woo Nam, Daniel Oblak, and Wolfgang Tittel. Quantum storage of entangled telecom-wavelength photons in an erbium-doped optical fibre. *Nature Photonics*, 9(2):83–87, January 2015.

[26] K. Garay-Palmett, D. Cruz-Delgado, F. Dominguez-Serna, E. Ortiz-Ricardo, J. Monroy-Ruz, H. Cruz-Ramirez, R. Ramirez-Alarcon, and A. B. U'Ren. Photon-pair generation by intermodal spontaneous four-wave mixing in birefringent, weakly guiding optical fibers. *Phys. Rev. A*, 93:033810, Mar 2016.

[27] D. Cruz-Delgado, R. Ramirez-Alarcon, E. Ortiz-Ricardo, J. Monroy-Ruz, F. Dominguez-Serna, H. Cruz-Ramirez, K. Garay-Palmett, and A. B. U'Ren. Fiber-based photon-pair source capable of hybrid entanglement in frequency and transverse mode, controllably scalable to higher dimensions. *Scientific Letters*, 6(27377), Jun 2016.

[28] S. Warier. *The ABCs of Fiber Optic Communication*. Artech House, 2017.

[29] Guide to Fiber optics and Premises Cabling. *https://www.thefoa.org/ESP/Fibra_optica.htm*.

[30] K. Okamoto. *Fundamentals of Optical Waveguides*. Academic Press, 2006.

[31] R. W. Boyd. *Nonlinear optics*. Academic Press, 2006.

[32] Y. R. Shen. *The principles of nonlinear optics*. Wiley-Interscience, 2003.

[33] Y. Shen. Basic considerations of four-wave mixing and dynamic gratings. *IEEE Journal of Quantum Electronics*, 22(8):1196–1203, 1986.

[34] O Alibart, J Fulconis, G K L Wong, S G Murdoch, W J Wadsworth, and J G Rarity. Photon pair generation using four-wave mixing in a microstructured fibre: theory versus experiment. *New Journal of Physics*, 8(5):67, may 2006.

[35] C C. Gerry and P L. Knight. *Introductory quantum optics*. Cambridge Univ. Press, 2004.

[36] Fumihiro Kaneda, Karina Garay-Palmett, Alfred B. U'Ren, and Paul G. Kwiat. Heralded single-photon source utilizing highly nondegenerate, spectrally factorable spontaneous parametric downconversion. *Opt. Express*, 24(10):10733–10747, May 2016.

[37] I. H. Malitson. Interspecimen comparison of the refractive index of fused silica∗,†. *J. Opt. Soc. Am.*, 55(10):1205–1209, Oct 1965.